Fibrin structural and diffusional analysis suggests that fibers are permeable to solute transport

Kimon Alexandros Leonidakis[1, 2], Pinaki Bhattacharya[1], Jennifer Patterson[2, 3], Bart E. Vos[4], Gijsje H. Koenderink[4], Jan Vermant[5, 6], Dennis Lambrechts[2, 7, 8, ¶], Maarten Roeffaers[8, ¶], Hans Van Oosterwyck[1, 2, ¶, *]

[1]Biomechanics Section, KU Leuven, Leuven Belgium

[2]Prometheus, Division of Skeletal Tissue Engineering, KU Leuven, Leuven, Belgium

[3]Department of Materials Engineering, KU Leuven, Leuven, Belgium

[4]Biological Soft Matter Group, FOM Institute AMOLF, Amsterdam, the Netherlands

[5]Department of Chemical Engineering, KU Leuven, Leuven, Belgium

[6]Department of Materials, ETH Zurich, Zürich, Switzerland

[7]Skeletal Biology and Engineering Research Center, KU Leuven, Leuven, Belgium

[8]Center for Surface Chemistry and Catalysis, KU Leuven, Leuven, Belgium

[¶]These authors share senior authorship

[*]Corresponding author. Celestijnenlaan 300C –Box 2419, 3001 Leuven, Belgium

Abstract

Fibrin hydrogels are promising carrier materials in tissue engineering. They are biocompatible and easy to prepare, they can bind growth factors and they can be prepared from a patient's own blood. While fibrin structure and mechanics have been extensively studied, not much is known about the relation between structure and diffusivity of solutes within the network. This is particularly relevant for solutes with a size similar to that of growth factors. A novel methodological approach has been used in this study to retrieve quantitative structural characteristics of fibrin hydrogels, by combining two complementary techniques, namely confocal fluorescence microscopy with a fiber extraction algorithm and turbidity measurements. Bulk rheological measurements were conducted to determine the impact of fibrin hydrogel structure on mechanical properties. From these measurements it can be concluded that variations in the fibrin hydrogel structure have a large impact on the rheological response of the hydrogels (up to two orders of magnitude difference in storage modulus) but only a moderate influence on the diffusivity of dextran solutes (up to 25% difference). By analyzing the diffusivity measurements by means of the Ogston diffusion model we further provide evidence that individual fibrin fibers can be semi-permeable to solute transport, depending on the average distance between individual protofibrils. This can be important for reducing mass transport limitations, for modulating fibrinolysis and for growth factor binding, which are all relevant for tissue engineering.

Keywords

Fibrin hydrogels; Structural characterization; Diffusion; Rheology; Fiber permeability

1. Introduction

Hydrogels are an interesting class of biomaterials, with mechanical, biochemical and transport properties that can be tailored to the needs of a specific application [1–5]. This makes them promising candidates as extracellular matrix (ECM) substitutes in tissue engineering, because they can offer mechanical support to cells while providing necessary signals for the development of new tissue. Structural cues are important as they influence cell behavior [6], and matrix stiffness is also known to

mediate cell fate [7] with mechanical properties of the substrate having an impact on cell behavior in terms of morphology [8], migration [9] and differentiation [10]. At the same time, microstructural and mechanical properties may affect cell behavior through similar mechanisms, as variations in structure induce mechanical changes to the cells [11]. Therefore, making a clear distinction between the influence of microstructure and mechanical properties is not straightforward. Mass transport properties of the ECM are important because they influence local solute concentrations and their gradients, thereby modulating cell behavior and multicellular organization, during development and tissue regeneration, such as part of a tissue engineering strategy [12]. Knowing the diffusivity of a solute within a carrier material gives information not only on the local transport processes of the solutes but also on the release kinetics of the system. Therefore, solute diffusivity can be used as a marker for the potential of a carrier to release embedded growth factors and other proteins [13]. Hence, it is clear that a combination of the desired structural, transport and mechanical properties of a scaffold is of great importance for tissue engineering applications.

Fibrin hydrogels are natural biomaterials which have been used in tissue engineering for multiple applications, such as in skin, cartilage, bone and vascular regeneration [14]. The fibrin clot is the natural product of the coagulation cascade. Fibrinogen, the precursor protein to fibrin, is a 340,000 Da glycoprotein comprised of three nodules with a total length of 45 nm. Thrombin (factor IIa), a protease, cleaves the fibrinopeptides A and B from the fibrinogen molecule resulting in fibrin monomers that spontaneously polymerize once they are formed [15]. Fibrin hydrogels exhibit a fibrous structure which has been the subject of many studies [16–19] and encompasses a range of scales, as illustrated in Fig. 1. Thrombin, calcium, fibrinogen, pH and ionic strength are all known to influence the geometrical features of the fibrous mesh, mainly by changing the radius and average length of the individual fibers, the branch density, as well as molecular packing density of the fibers. For example, it is well known that the total fiber length and the fiber diameter are inversely proportional to thrombin concentration [20]. These observations can be linked to fibrin polymerization kinetics, as thrombin acts as a promoter of the polymerization and a decrease in the thrombin to fibrinogen ratio leads to increased lateral aggregation of the protofibrils and a larger fiber radius [17].

Ionic strength [18], specifically the concentrations of calcium [21] and chloride ions [22] also have an effect on structure. Finally, changes in factor XIIIa concentration have been shown to affect the packing of protofibrils within the fibers, with higher concentrations of factor XIIIa leading to fibers with a smaller distance between the constituent protofibrils [23].

Besides playing an important role in hydrogel structure and mechanical properties, these factors are also known to affect solute transport within fibrin hydrogels [24–26]. Hydrogels, as the name implies, are materials that mainly consist of water. In the case of fibrin, water exists not only in the space between fibers but also within the individual fibers that constitute the hydrogel. It has been estimated that only a small part of the actual fiber volume, between 10 and 30 vol %, is occupied by the protein with the rest being taken up by water [18,27,28]. Several studies have focused on unraveling the details of the internal fiber structure, showing that it is strongly influenced by the concentrations of fibrinogen and thrombin as well as the ionic strength during polymerization [17,18,27].

The fact that water is the main constituent of fibrin fibers can also cause complications when measuring the fiber thickness by certain techniques. For example, scanning electron microscopy (SEM), involves a dehydration step in the preparation of the samples. This step is likely to cause fiber shrinkage, hampering a straightforward extraction of the fiber radius, although SEM still provides valuable quantitative information about the average length of the fibers or the branch density [29]. Turbidimetry on the other hand is a non-invasive technique, which is based on the Rayleigh scattering theory, to characterize fibrin hydrogels in the native hydrated state [30]. Starting from the assumption that the hydrogel consists entirely of an isotropic collection of rigid rods, turbidimetry relates changes in optical absorbance over a range of wavelengths with the diameter and mass-length ratio of the fibers. However, the analysis critically relies on several assumptions to relate light scattering to hydrogel structural properties as these are not directly observed, and literature findings until now have mainly been limited to hydrogels of rather low fibrinogen concentrations (less than 2 mg/mL) [18,19,30]. Confocal microscopy has mainly been used to quantify pore sizes in fibrin hydrogels [31,32]. Determination of fiber diameters is difficult since values of the fiber diameter typically fall well below 200 nm and therefore below the diffraction-limited spatial resolution of (non-

superresolution) optical microscopy. Therefore, measurement of fiber thickness based on optical microscopy images is not trivial and relies on mathematical approximations based on the point spread function of the microscope [33]. In this study we overcome the drawbacks of the individual methods by implementing a novel combined approach, using confocal fluorescence microscopy and turbidimetry to quantitatively analyze different fibrin compositions.

The complexity of fibrin hydrogels is not only limited to their structure, but it is also evident in their mechanical behavior, which also depends on the fibrin composition [23] and therefore on the structural details of the hydrogel [34,35]. Dilute fibrin networks (0.5-8 mg/mL) exhibit a complex nonlinear elastic response with a transition from entropic elasticity at small strains to enthalpic elasticity at large strains [34]. The storage modulus in the linear elastic regime is well-described by entropic models valid for semiflexible polymers [36], being governed by the total fiber length and the fiber persistence length, which in turn is dependent on the number of protofibrils per fiber. Dense fibrin networks with small fiber segment lengths between junctions and networks of thick fibers behave as athermal fibrous networks even at low strain [37,38].

Diffusivity of solutes through fibrin hydrogels has been studied to assess the influence of cell density on the diffusion of small molecules such as Rhodamine B (4 mg/mL fibrinogen) [39] and the influence of mechanical strain on anisotropic diffusion [40]. Novel experimental setups have been developed to probe the diffusion of insulin-like growth factor I (IGF-I) and ribonuclease through fibrin hydrogels of low density (2.25 mg/mL) and low volume fraction (0.27 vol% of a dry hydrogel), yielding diffusivity values comparable to that in water and pointing to a negligible influence of the open, fibrous network [41]. Moreover, variations in fibrinogen (5-20 mg/mL) and thrombin (2-20 U/mL) concentrations have been shown to affect the permeability of fibrin hydrogels and the release of dextran solutes (3 and 70 kDa) [42]. However, to the best of our knowledge, a quantitative analysis assessing the effect of specific fibrin hydrogel architectures on solute diffusivity over a wide range of pore sizes has not been tested so far. Moreover, although it has been shown that void spaces in-between protofibrils within the fibrin fibers can serve as “nanocavities” that could entrap therapeutic agents [43], there has not been a quantitative assessment of the effect of intrafibrillar structure on the diffusion of solutes. Whether or

not solutes can diffuse through individual fibers has remained an open question since it was stated in a seminal paper on fibrin formation [44], even though intrafibrillar diffusion has been demonstrated and measured for collagen [45].

In this study we demonstrate that structural variations have a profound impact on the mechanical properties of the hydrogels but only a moderate influence on solute transport. The in-depth, quantitative characterization of the hydrogel architecture was derived from confocal fluorescence imaging in combination with a fiber extraction algorithm and this information was complemented with turbidimetry for individual fiber characterization. Based on combined results from the structural and diffusional characterization, we provide evidence that individual fibrin fibers can be permeable to small solutes under assembly conditions that promote a porous fiber structure.

2. Materials and Methods

2.1 Fibrin hydrogel preparation

Fibrin hydrogels were prepared by mixing fibrinogen and thrombin components in equal volumes (pH=6.6). Plasminogen depleted fibrinogen (Enzyme Research Laboratories, USA) derived from human plasma, was dissolved in a 20 mM HEPES and 150 mM NaCl, fibrinogen buffer. Stock solutions of thrombin (Sigma, USA), derived from human plasma, and factor XIII (Fibrogammin, CSL Behring, Germany) were prepared using a 20 mM HEPES, 150 mM NaCl, 40 mM CaCl and 0.1% BSA thrombin buffer and pure water, respectively. Thrombin and factor XIII were mixed with the thrombin buffer and were kept in a waterbath at 37°C for 30 minutes in order to activate factor XIII to factor XIIIa. Fibrinogen and thrombin components were thoroughly mixed to a total volume of 60 μL and pipetted directly on a 24 imaging well plate (Cellvis). Subsequently, the hydrogels were left to polymerize for 60 minutes at 37°C in a 100% humid environment and then PBS was added in each well to keep the gels hydrated. The samples were left at room temperature for at least 15 hours before further measurements.

Compositions were selected based on a 3-parameter, mixed-level full factorial design. Fibrin hydrogels derived from three different fibrinogen concentrations (final concentrations of 5, 10 and 20 mg/ml), which are typically used in tissue engineering applications [46–48], were investigated in this study. As thrombin and factor XIII act as enzymes on fibrinogen for the formation of fibrin, the weight concentration ratios of thrombin and factor XIII to fibrinogen were kept constant when changing the fibrinogen concentration. However, because of the reconstitution of factor XIII in pure water, the salt concentrations of the final gels were not constant for the high factor XIII compositions. Details on the concentrations of each constituent are presented in Table 1. For each fibrinogen concentration, we considered the influence of a 10-fold difference in thrombin concentration (Low = 0.02 and High = 0.2 U/mg fibrinogen) and a 100 fold difference in factor XIII concentration (Low = 0.02 and High = 2 U/mg fibrinogen) on the fiber organization and mechanical properties of the gels, as well as the diffusion of dextran probes. Moreover, a steady decrease in $CaCl_2$ (20-4 mM; see Table 1) while increasing the fibrinogen concentration allowed us to assess the combined effect of $CaCl_2$ and factor XIII concentrations. For visualizing the internal fibrous structure of fibrin hydrogels with confocal microscopy, fluorescent fibrin hydrogels were prepared for the same compositions described in Table 1, using fibrinogen conjugated with Alexa Fluor 488 (Sigma) at 2% of the total weight of fibrinogen in solution. A three-parameter, two-level factorial design, using the lowest (5 mg/mL) and the highest (20 mg/mL) fibrinogen concentrations as the two extreme cases, was used to assess differences in the rheological response of the hydrogels.

2.2 Confocal fluorescence imaging

Images of fluorescent hydrogel networks were acquired on an inverted confocal laser scanning microscope (Olympus Fluoview 1000) equipped with a 60x water immersion objective (UPLSAPO, NA=1.20), with a pixel dwell time of 200 μs and a pinhole size of 69 μm. Image stacks were obtained covering a total volume of 25.6 × 25.6 × 6.08 μm^3 with a voxel size of 50 × 50 × 160 nm^3. All images were taken approximately 30 μm deep in the gel. The image stacks were further processed using the fiber extraction algorithm described below.

2.3 Fiber extraction algorithm

A detailed description of the 3D analysis including image processing steps and fiber extraction routines is presented in Supporting Material. In brief, multiple slices of image stacks (Fig.2a) acquired by confocal fluorescence microscopy were processed in several steps (Fig. 2b) following which the network topology was extracted using the FIRE algorithm [49], for an optimized set of parameters (Fig. 2c). The extracted network (Fig. 2d) was then analyzed for fiber and network characteristics, such as average fiber length and total fiber length, hydrogel fiber density and branch density (see Tables 2 and 3 for a full list of characteristics).

2.4 Turbidimetry

Turbidity measurements were used to quantitatively describe network characteristics, based on a method developed by Carr and Hermans [30] and later elaborated by Yeromonahos et al. and Piechocka et al. [18,34]. Given the spectral range of the measurement (λ_1 - λ_2) the method works under the assumption that fibrin hydrogels consist of a network of randomly oriented, thin ($r_f << \lambda_1$) and long ($L >> \lambda_2$) cylindrical fibers [19]. Then the mass to length ratio (μ) and the average radius (r_f) of the fibers can be estimated as [23]:

$$t\lambda^5 = A\mu(\lambda^2 - Br_f^2) \tag{1}$$

where

$$A = (88/15)c\pi^3 n_s \left(\frac{dn}{dc}\right)^2 (1/N_A) \tag{2}$$

$$B = (184/231)\pi^2 n_s^2 \tag{3}$$

$t = OD\ l\ ln(10)$, λ is the wavelength, OD is the optical density, l is the path length in cm, n_s is the refractive index of the solvent, dn/dc is the specific refractive index increment for fibrin (= 0.17594 cm^3/g) [18], c is the fibrinogen concentration in g/mL and N_A is the Avogadro number. In the wavelength range of 500-800 nm the dependence of $t\lambda^5$ to λ^2 is typically linear and the slope of that line gives μ, while the intercept is dependent on both μ and r_f. Knowing the mass to length ratio of the protofibrils, $\mu_0 = 1.44 \cdot 10^{11}$ Da/cm [17] one can calculate the average number of protofibrils as $N_p = \mu/\mu_0$, while the fiber internal density can be estimated as

$$\rho_f = \mu / N_A \pi r_f^2 \tag{4}$$

Since the concentration of fibrinogen is defined as c = mass of protein/volume of the hydrogel and the fiber internal density as ρ_f = mass of protein/volume of the fiber, we can therefore define the fiber volume fraction as the percentage of volume occupied by the fibrin fibers within the total volume of a hydrogel:

$$\Phi = \frac{c}{\rho_f} = \frac{cN_A \pi r_f^2}{\mu}$$

$$\Phi = \frac{cN_A \pi r_f^2}{N_p \mu_0} \tag{5}$$

Turbidity measurements were performed with a spectrophotometer (Shimadzu, UV1650PC) within a wavelength range of 350-1000 nm. Fibrin hydrogels for each composition ($n \geq 3$) were mixed and left to polymerize in disposable cuvettes (Eppendorf UVettes) at 37°C for 1h in a humidified environment. Subsequently, PBS was added, and the top of each cuvette was covered with parafilm to keep the samples hydrated overnight at room temperature. The next day, measurements were performed with a 0.5 nm wavelength increment. To compensate for the high fibrinogen concentrations (5-20 mg/mL), the 2 mm path length was used instead of the standard 10 mm. For all samples there was a linear relation between $t\lambda^5$ and λ^2 in the 500-800 nm wavelength range (Fig. S1). Therefore, this range was used for further analysis except for the hydrogels of 10LL, 10HL, 20LL and 20HL where a range of

700-1000 nm was retained, as at smaller wavelengths there was significant noise due to the high turbidity of the samples.

Total fiber length (ρ_L, defined per unit of hydrogel volume) cannot be directly estimated from the turbidity measurements. However, assuming that fibers are cylindrical and knowing the average fiber radius and the fiber volume fraction of each composition, total fiber length can be calculated as follows:

$$\Phi = \frac{V_{fib}}{V_{tot}} = \frac{\pi r_f^2 L}{V_{tot}} = \pi r_f^2 \rho_L$$

so that:

$$\rho_L = \frac{\Phi}{\pi r_f^2} \tag{6}$$

with V_{tot} the volume of the hydrogel imaged via confocal microscopy, V_{fib} the total fiber volume within the same hydrogel volume and L the total length of all cylindrical fibers. In this manner, a direct comparison between the fiber extraction algorithm and turbidimetry was possible via the cross-validation of ρ_L obtained from each method.

Following Yeromonahos et al. [18], the distance between protofibrils is calculated starting from their packing geometry. Protofibrils are expected to take a hexagonal close packing formation as cylinders within the fiber bundle [44]. The protofibril volume fraction (protofibril volume/fiber volume) would then be:

$$\Phi_{pf} = \frac{\pi}{2\sqrt{3}} \tag{7}$$

Assuming that each protofibril stands in the center of a cylinder of radius $r_c/2$ and height h, the distance between the centers of two protofibrils equals r_c. Then the protofibril volume fraction can be calculated as:

$$\Phi_{pf} = \frac{h\pi\left(\frac{r_c}{2}\right)^2 N_p}{h\pi r_f^2} \tag{8}$$

Equating (7) and (8) yields:

$$r_c = \sqrt{\frac{2\pi r_f^2}{N_p\sqrt{3}}} \tag{9}$$

Finally, the end-to-end distance between the surfaces of adjacent protofibrils, i.e. protofibril distance, is

$$d_{pf} = r_c - r_{pf} \tag{10}$$

with r_{pf} = 6.7 nm the protofibril diameter [17].

2.5 Fluorescence recovery after photobleaching (FRAP)

FRAP experiments were performed to assess the influence of various fibrin formulations on the diffusive transport of solutes. As a model solute, dextran-FITC (Sigma), a highly branched globular polysaccharide was used. In particular, molecular weights of 10 and 40 kDa were used, as these sizes are similar to those of growth factors of interest for tissue engineering. Fluorescein isothiocyanate (FITC) is randomly conjugated to the dextran backbone at concentrations ranging from 0.003 to 0.02 mole FITC per mole of glucose. The approximate hydrodynamic radii for the two solutes are 2.3 nm for 10 kDa and 4.5 nm for 40 kDa, as provided by the manufacturer. The solutions were diluted in PBS to a final concentration of 100 μM for 10 kDa and 50 μM for 40 kDa dextran.

Diffusivity within the fibrin hydrogels is expressed here in terms of relative diffusivity, or D/D_0, where D is the diffusion coefficient in the hydrogel and D_0 is the diffusion coefficient in PBS. The experimental procedure has been described in detail previously [50]. Briefly, a selected region in a solution containing the fluorescent solute was photobleached and subsequently the fluorescence recovery within this region was monitored. By fitting analytical solutions of Fick's second law to the obtained recovery curve, the diffusion coefficient could be derived.

In our experiments we used an inverted confocal microscope (Olympus Fluoview 1000) with a 10x air objective (UPLSAPO, NA = 0.40). The pixel size was set to 0.355 × 0.355 μm^2 and images of 512 × 512 pixels were recorded which yielded a 181.76 × 181.76 μm^2 field of view. The photobleached region was defined as a circle with a diameter of 35.5 μm, with a bleaching time of 500 ms. For each measurement a time series of 18.27 s or 70 images for 10 kDa and 25.89 s or100 images for 40 kDa was recorded. In these time series the first five images were used to establish the background intensity before bleaching. All measurements were performed at 37°C at a depth of approximately 30 μm inside the hydrogel (measured from the glass bottom of the imaging well plate) to avoid surface artifacts. For every hydrogel composition 6 samples were tested, using for each replicate the average value of 5 measurements performed on different regions of the examined hydrogel. The experiments were performed on different days for two sets of triplicates for each composition in order to avoid possible systematic errors.

FRAP experiments were analyzed using an algorithm [51] that implements image averaging and spatial frequency analysis for improved accuracy of measurements with occasional heterogeneities or non-ideal signal to noise ratio (Fig. S4). The diffusion coefficients of 10 and 40 kDa dextran solutes in PBS buffer (147.3 ± 2.1 and 73.7 ± 3.5 μm^2/s, respectively) were obtained experimentally via FRAP and they are in good agreement with the Stokes-Einstein (S-E) equation:

$$D = \frac{k_B T}{6\pi\eta r_s} \tag{11}$$

where k_B is the Boltzmann's constant (J/K), T is the temperature (K), η is the dynamic viscosity of the solvent (Pa·s) and r_s is the hydrodynamic radius (m) of the solute. The predicted values for passive diffusion in water from S-E equation were 143 μm^2/s for 10 kDa and 73 μm^2/s for 40 kDa dextran.

2.6 Model of molecular diffusion in hydrogels

Obstruction models are often used to rationalize molecular diffusion in hydrogels. Such models are based on the assumption that interactions between solutes and the solid part of the hydrogel are steric

in nature. This means that the fibers are considered merely as obstacles for solute diffusion, effectively increasing the total path and hence decreasing the effective macroscopic diffusion coefficient. For the hydrogels used in this work the obstruction models are most suitable, since the solute radius is much smaller than the fiber radius ($0.019 < r_s/r_f < 0.065$), thus no solute-solute or solute-fiber interactions are expected. The model of Ogston [52] focuses on the obstruction effects, but in addition to the volume fraction (Φ) it also incorporates the solute radius (r_s) and fiber radius (r_f):

$$\frac{D}{D_0} = \exp\left(-\frac{r_s+r_f}{r_f}\Phi^{0.5}\right) \quad (12)$$

Here, the solutes are assumed to be 'hydrodynamically equivalent spheres', and the fibers are considered as long impermeable cylinders.

2.7 Shear rheometry

All 5 and 20 mg/mL fibrinogen compositions (8 compositions in total, see Table 1) were tested under small-amplitude oscillatory shear (SAOS) rheometry in order to measure the storage and loss shear moduli. Three types of tests were conducted: time-sweep, strain amplitude-sweep and frequency sweep. For each test type, results from 3 samples per composition were averaged. Time sweeps and strain sweeps were performed for 4 compositions in order to estimate the time needed for the hydrogel to reach a steady state (t_s) and the linear region of strain amplitude (γ_{LVE}). This information was then further used in the frequency-sweep tests that were performed at the same polymerization time and strain amplitude for all 8 compositions. A Physica MCR 501 rheometer (Anton Paar GmbH, Austria) was used with a parallel-plate set-up and a Peltier system and a hood for temperature control. Immediately after dispensing a 200 μL drop of unpolymerized solution on the bottom plate (pre-cooled to 15°C), a 20 mm diameter top plate was lowered from an initial gap of 20 mm to a final gap of 0.5 mm (final gaps of 2 mm were also tested for a few samples and the rheological response was shown to be independent of the gap distance). After the top-plate reached the final gap, the temperature of the bottom plate was raised to 37°C. Next, heavy mineral oil was poured over the

exposed surface of the gel to reduce evaporation, and in addition a solvent trap was placed over the entire setup. This point in time was defined as the time origin (t=0).

In the time-sweep tests, starting at t = 0 oscillations were performed at a (engineering) strain amplitude γ = 1% and angular frequency ω = 1 rad/s. The value of the storage modulus G' was monitored continuously at 10 s intervals as it increased and asymptotically reached a steady state. The time-sweep curves (variation of G' with time t) resulted in the determination of time of steady state t_s. In particular, t_s was defined as the first instant (rounded up to a multiple of 20 minutes) when the slope $\dot{G}$ = dG′/dt dropped below 2.1% of its maximum attained value (see Supporting Material C).

In the strain amplitude-sweep tests, the gel was allowed to polymerize for the 'at-rest' duration $0 < t < t_s$ with exact t_s depending on each composition. After this duration a fixed frequency (ω = 1 rad/s) oscillation was applied with γ increasing from 0.01% – 100%. A linear viscoelastic (LVE) region was determined by the condition that inside the LVE G′ varies by less than 10%.

In the frequency-sweep tests, similar to the strain amplitude-sweep test, fibrin was allowed to polymerize at rest initially for a duration t_s. Next, at a fixed strain amplitude value selected from within the LVE (γ_{LVE}), oscillation was applied with ω decreasing from 100 rad/s to 0.01 rad/s.

2.8 Statistical analysis

All statistical analysis was performed in R. For the results derived from the fiber extraction algorithm Tukey and Games-Howell multiple comparison tests were performed. Significant differences in the diffusivity study were assessed with Tukey, and for turbidimetry Games-Howell was used due to the differences in sample sizes and heteroscedasticity of the data. Equality of variances was assessed using Levene's test.

3. Results

3.1 Fibrin hydrogel network characterization

The hydrogel structure was initially studied using confocal fluorescence microscopy. Fig. 3 shows a typical single image from the 3D image stacks as obtained for every examined composition (see Table 1). As expected, the individual fibrin fibers are randomly oriented within the fibrin hydrogels. The network structure is strongly dependent on the hydrogel composition and highly concentrated fibrin hydrogels (20 mg/mL) show a very dense appearance. In two of these hydrogels (20LH and 20HH) it is difficult to discern individual fibers due to the diffraction-limited resolution. Focusing more on the hydrogel appearance it is clear that for a given thrombin and factor XIII concentration, i.e. within a column of images in fig. 3, the hydrogel fiber density increases with higher fibrinogen concentrations. At the same time, for a given fibrinogen concentration, i.e. within a row of images in fig. 3 compositions with higher thrombin and/or factor XIII concentrations tend to yield a higher hydrogel fiber density and a higher branch density.

The confocal fluorescence images alone give a clear but qualitative view of the hydrogel architecture for the different fibrin compositions. In order to obtain quantitative information from the three-dimensional image stacks a fiber extraction algorithm was implemented. This allowed for the deduction of five structural parameters, mainly fiber network properties (see also Fig. 1 and Tables 2 and 3): average fiber length, total fiber length, hydrogel fiber density, branch density and fiber connectivity, shown in Fig. 4.

Because the hydrogel fiber density of the 20LH and 20HH hydrogels exceeded the diffraction-limited resolution, fiber network characteristics could not be extracted. Average fiber length, total fiber length, hydrogel fiber density and branch density were all found to be significantly higher for compositions with higher fibrinogen concentrations in cases with the lower factor XIII concentration (LL and HL; Fig. 4a-d). Increased concentrations of thrombin increased the hydrogel fiber density for the same fibrinogen concentrations in all cases (Fig. 4c) and also increased total fiber length and branch density, even though these differences were not significant for all fibrinogen concentrations (Fig. 4b and d).

Fiber connectivity was not affected by variations in fibrin constituents, except for 10LH composition (Fig. 4e). Variations in fibrinogen concentration had a bigger impact on network characteristics related to total fiber number than on average fiber length: total fiber length, hydrogel fiber density and branch density showed a 4.1, 3.1 and 3.1-fold increase respectively, for a 4-fold increase in fibrinogen concentration (from 5 to 20 mg/mL), compared to only a 33% increase in average fiber length (LL compositions). On the other hand, the branch density was most influenced by a 10-fold increase in thrombin concentration with up to 81% more branches in 5HL compared to 5LL, followed by 57% increase of hydrogel fiber density and 56% increase of total fiber length for the same conditions.

To complement the data obtained from the confocal images in combination with the fiber extraction algorithm and in particular for a better view into individual fiber characteristics (Fig. 1 and Table 3), turbidimetry was used. Apart from fiber radius (Fig. 5a) which is difficult to be correctly estimated from the confocal images, the other structural features obtained were the number of protofibrils (Fig. 5b), fiber internal density (Fig. 5c) and fiber volume fraction (Fig. 5d).

The fiber radius was found to significantly decrease with increasing thrombin concentration for 10 mg/mL fibrinogen and between 20LL and 20HL (Fig. 5a). Variations in fibrinogen concentration did not influence fiber radius at high thrombin concentrations (HL and HH compositions), while it led to significant differences at low thrombin concentrations. The number of protofibrils was significantly different between compositions with different factor XIII concentrations. Other significant differences in numbers of protofibrils were found between 5LH, 10LH and 20LH on the one hand and between 5HH, 10HH and 20HH on the other hand. In particular, one can notice the rather low numbers (~25-28) of protofibrils for the 20LH and 20HH compositions (Fig. 5b). In general, differences in numbers of protofibrils cause differences in fiber internal density (Fig. 5c) and fiber volume fraction (Fig. 5d) between compositions of low versus high factor XIII and differences between compositions with different fibrinogen concentrations. One of the most striking results is the very high fiber volume fraction for 20LH and 20HH (Fig. 5d).

The structural characteristics of fibrin hydrogels were determined by two independent techniques, turbidimetry and confocal fluorescence imaging with fiber extraction algorithm. A direct comparison between the results of both approaches in terms of total fiber length can be seen in Fig. 6. The data are in good agreement for low fibrinogen concentrations (5 mg/mL), while some discrepancies are found for 10LH, 10HH and 20HL compositions that can be attributed to the diffraction limited resolution of the confocal fluorescence imaging in combination with the large hydrogel fiber density in the hydrogel networks. At the same time, the turbidimetry analysis requires that $r_f << \lambda$ and fiber length $L >> \lambda$ and that fibers are monodisperse. Moreover, there is no direct observation of the structure that can serve as quality control over the results it yields. Hence, cross-validation of the two methods suggests that the results from turbidity measurements can be trusted over this range of fibrinogen concentrations.

3.2 Diffusivity of dextran solutes

Diffusion coefficients of FITC-conjugated 10 kDa and 40 kDa dextran were measured by FRAP for the different fibrin compositions and normalized with respect to the diffusion coefficient of the same molecular weight dextran measured in PBS. Results presented in Fig. 7 demonstrate that relative diffusion coefficients tend to decrease with increasing fibrinogen concentration for all enzyme concentrations. Statistical analysis of the results showed that large differences in fibrinogen concentration (5 versus 20 mg/mL) led to significant differences in diffusivity. The lowest diffusion coefficients were found for the 20LH and 20HH compositions both for 10 and 40 kDa dextran. Overall, fibrinogen concentration was found to be the most important parameter affecting dextran diffusivity for both solutes, but changes in the enzyme composition at the same fibrinogen concentrations significantly influenced diffusivity of the larger solute as well.

A comparison of the experimental data with values predicted from the Ogston model suggests that the model does not adequately explain the observed relative diffusivities (Fig. 7b and d). The Ogston model tends to predict lower diffusivity values, which can be explained by an overestimation of the effect of fiber volume fraction. This can also be appreciated from the larger data range for

experimental values than for predicted values (see bounding box in Fig. 7b and d). These discrepancies are most pronounced for the 20LH and 20HH compositions (cases in circles), which exhibit the highest fiber volume fractions (Fig. 5d).

3.3 Shear rheometry

Time-sweeps were performed in order to find the time when polymerization reached a steady-state. Results of the time-sweep measurements are presented in Fig. 8a. 5LL showed the slowest progress in polymerization while the other compositions which have at least one of the two enzymes (thrombin or factor XIII) in more elevated concentrations showed faster polymerization times. The time required for the storage modulus to reach a steady-state (t_s) was found to be 4800 s for compositions 5LL and 5HH, 6000 s for 20LH and 7200 s for 20HL. For the remaining compositions 5LH, 5HL, 20LL, 20HH, in frequency-sweep measurements the t_s was kept to this maximum (7200 s) in order to ensure that the hydrogels had adequately polymerized. Strain amplitude sweep tests were performed to assess the linear viscoelastic region of the fibrin hydrogels. All compositions exhibited a constant G' value for strain amplitudes up to 4% for 5LL, 10% for 5HH and 16% for 20LH and 20HH (Fig. 8b). In order to keep the measurements within the linear viscoelastic regime while giving a good signal to noise ratio, the frequency-sweep measurements were carried out at 1% strain amplitude for all 8 compositions.

Frequency sweep measurements were performed for all compositions of 5 and 20 mg/mL fibrinogen, in order to assess the influence of hydrogel structure on the shear rheological response. The results show a frequency-independent G' value for all samples, characteristic of a nearly perfect, elastic solid (Fig.8c). Therefore, average G' values at 1 rad/s frequency were compared between different compositions (Fig. 8d). Higher fibrinogen concentrations resulted in higher G' values for all enzyme ratios, with striking differences in the rheological response of hydrogels of equal fibrinogen concentrations but different enzyme concentrations. LL compositions exhibited the highest shear storage modulus and HL the lowest for both fibrinogen concentrations. For example, there was a more than 20-fold difference between 5LL (313 Pa) and 5HL (14.5 Pa) and more than 8-fold between 20LL

(2283 Pa) and 20HL (269 Pa). The loss modulus (G") was found to follow the same trend between different hydrogel compositions but with different response to changes in frequency, showing increased values at higher frequencies (Fig. 8e). The loss tangent (tanδ) shows the ratio of energy dissipated over the energy stored in the studied system (Fig. 8f). The variations between compositions at 1 rad/s were relatively small, but the tanδ values increased for lower (5LL and 5HH) and higher frequencies (all compositions).

A quantitative description of the influence of structural properties (e.g., fiber radius, total fiber length, branch density, number of protofibrils, etc.) on rheological properties could not be captured by a single power law model. We attempted to find an empirical expression of the form $G' = A\, x^a y^b z^c$ with x, y and z values of structural properties and A, a, b and c unknown parameters that were determined by means of least squares optimization (Matlab). The structural parameters were selected one at a time from three groups: intrafibrous (i.e., number of protofibrils and fiber internal density), individual fiber (i.e., fiber radius and average fiber length) and hydrogel network properties (i.e., total fiber length, hydrogel fiber density, fiber volume fraction and branch density) at different combinations. However, none of these models were able to fit the entire set of experimental results (data not shown).

4. Discussion

4.1 Fibrin composition affects individual fiber and network characteristics

A novel methodological approach has been followed for the quantification of network and individual fiber properties of dense fibrin hydrogels (as defined in Tables 2 and 3 and illustrated in Fig. 1). By combining confocal fluorescence microscopy with a fiber extraction algorithm and turbidimetry the obtained results can be cross-validated. Fibrinogen, the main fibrin hydrogel precursor, not only determines the total fiber length, but also the hydrogel fiber density, as an increase in fibrinogen concentration was observed to result in higher values for both network characteristics (Fig. 4b and c, respectively). Further, the hydrogel fiber density also positively correlates with the branch density

(Fig. 4d) as expected from the kinetically controlled fibrin polymerization process described earlier. Detailed hydrogel structural analysis also showed that fibrinogen concentration positively correlates with the average fiber length for low factor XIII compositions (see Table 1 and Fig. 4a).

Thrombin is responsible for the initiation of fibrin polymerization and an increased thrombin to fibrinogen concentration ratio is known to result in thinner fibers and a smaller number of protofibrils at the stage of fiber formation [17]. This is confirmed by our data (Fig. 5a and b, between LL and HL compositions) and can be rationalized by the role of thrombin during the polymerization process. Thrombin cleaves fibrinopeptides A and B from the fibrinogen molecule, initiating the formation of protofibrils and their lateral aggregation for the formation of fibrin fibers. However, protofibril formation happens more rapidly than lateral aggregation at high thrombin concentrations, while lateral aggregation is favored over protofibril formation at low thrombin concentrations [53]. Overall, values for fiber radii and the number of protofibrils are in line with those from literature [17,18,23,27] and the same trends were observed for the influence of thrombin on these two parameters (Fig. 5a and b) [17].

Furthermore, it has been reported that branch formation and lateral aggregation are essentially two opposite mechanisms [54] and we see this effect from increased thrombin on higher branch densities in Fig. 4d. In turn, higher branch densities should lead to increased total fiber lengths and hydrogel densities which are also evident in our analysis for increased thrombin concentrations (Fig. 4b and 4c, respectively). The fact that the total fiber length positively correlates with the hydrogel fiber density and the branch density but not with the average fiber length, also shows the influence of the polymerization process on the formation of the fibers. Fiber connectivity overall does not seem to be affected by changes in structure and the values obtained are in the same range with those from literature [20]. This suggests that generation of new fibers during polymerization always happens by the creation of new branch points and it is unrelated to the fibrin constituents.

The most remarkable differences observed were the high fiber volume fractions (up to Φ=0.57) of 20LH and 20HH compositions. This was primarily a result of these compositions possessing a very small number of protofibrils relative to the overall fibrinogen concentration. High fiber volume

fraction values have been reported before but for hydrogels of much higher fibrinogen concentration (Φ = 0.54 at 156 mg/mL) [26]. Similarly, low numbers of protofibrils (N_p = 2) have also been reported, but at high pH = 8.5 and salt concentrations of 400 mM NaCl [34]. Note that in this study 20LH and 20HH hydrogels were prepared with the lowest concentration of $CaCl_2$ compared to other conditions, only 4 μM (Table 1), which is in line with literature findings where an absence of Ca^{++} causes lower mass to length ratios [21] and consequently a lower number of protofibrils. Moreover, factor XIII is known to induce fiber compaction, and thus increase the number of protofibrils [23], which suggests that the observed differences in the number of protofibrils between low and high factor XIII concentrations are probably attributed to differences in the concentration of $CaCl_2$ and not factor XIII. Furthermore, the (weak) influence from factor XIII in compositions of 5 and 10 mg/mL fibrinogen, where the differences in $CaCl_2$ are smaller, also suggests that the observed differences in number of protofibrils, fiber internal density and fiber volume fraction at 20 mg/mL fibrinogen stem from the 5-fold difference in $CaCl_2$.

4.2 Effect of fibrin structure on diffusivity of dextran

Variations in individual fiber and network characteristics are responsible for different diffusion coefficients of dextran molecules within the hydrogels. This is particularly interesting for tissue engineering applications, as the solute sizes used here are in the same range as those of growth factors. In general, hindrance effects on solute relative diffusivity are moderate and are less than 25%, which is the biggest difference observed between highest and lowest diffusion coefficient (relative to lowest value) of all measurements performed with the same solute (here 5LH exhibits the highest and 20HH the lowest diffusivity for 40 kDa dextran). The largest differences in diffusivity have been demonstrated for compositions 20LH and 20HH (Fig. 7) which have the highest fiber volume fraction values, as seen in Fig. 5d. A graph of relative diffusivities plotted against fiber volume fraction values confirms their correlation (Supporting Material, Fig. S2). This is not surprising, because an increase in the fiber volume (solid) fraction of the hydrogel results in more steric interactions with the diffusing molecules. Apart from compositions 20LH and 20HH, diffusivity of 10 kDa dextran is not strongly

affected by modifications of the network except for differences in fibrinogen concentration (Fig. 7a) which positively correlates with total fiber length (Fig. 4b). Although these general remarks apply to 40 kDa dextran as well, changes in thrombin also become significant (Fig. 7b) because higher concentrations significantly increase hydrogel fiber density (Fig. 4c) without affecting the fiber internal density (Fig 5c), thus increasing the steric interactions between dextran and hydrogel fibers. Diffusivities of dextran molecules of both sizes seem to be independent of fiber radius when all compositions are accounted for, but when the outliers 20LH and 20HH are removed a negative correlation is revealed (Supporting Material, Fig. S3). For 40 kDa in particular, the radii of conditions with low thrombin concentration (LL and LH) and those with high thrombin concentration (HL and HH) appear to correlate independently with relative diffusivity. This is meaningful for the effect of structure on diffusion, given the fact that an increase in thrombin concentration led to an increase in total fiber length and hydrogel fiber density (Fig. 4b and c). As seen in Fig. S3 the compositions with increased thrombin show lower relative diffusivity values for the same fiber radii.

4.3 Fibrin fibers can be permeable to solute transport

A few models have been proposed for the internal protofibril packing structure within a fiber [18,27,44]. It was suggested that when the protofibrils are not tightly packed (i.e., at lower fiber densities), the crystalline structure of the protofibrils is maintained, but with defects (i.e., empty protofibril spaces) within the fiber. Individual fibers consist of protofibrils which occupy the space within as cylinders in hexagonal close packing [44]. The protofibril distances for the tested compositions in this study were in the range of 1.4 – 21.3 nm, with compositions 20LH and 20HH displaying the highest values. On the other hand, the hydrodynamic radii of 10 and 40 kDa dextran were 2.3 and 4.5 nm respectively, which makes fiber permeability a plausible hypothesis. Furthermore, the Ogston model was in agreement with the experimental results for some of the compositions which showed high fiber densities but not with others of lower fiber densities. Taking into account that in the Ogston model fibers are assumed to be impermeable, we hypothesized that the differences between experimental and predicted diffusivity values correlates to the end-to-end

protofibril distance (eq. 10). For instance, the fibers with tight protofibril packing, which exhibit essentially no void space between protofibrils, would not be expected to deviate from the model and thus give $(D/D_0)_{experimental} - (D/D_0)_{Ogston} = 0$. As one can see in Fig. 9, our data confirms this hypothesis.

The Ogston model [52] has been developed for the prediction of relative diffusivity of solutes within polymer networks with respect to the size of a solute, the fiber radius of the polymer network and the solid fraction in a system (equation 12) and is valid if the following criteria are fulfilled:

1. Solutes can be represented as hydrodynamically equivalent spheres, which is valid for dextran molecules in solution.
2. The specific volume of the fiber network should not change due to solute perturbation. Here, the size of dextran is in every case much smaller than the fiber thickness, thus it cannot affect the network specific volume.
3. The statistical distribution of the fibers is not affected by their own thickness or by the insertion of the solute. Effects are only expected when the total fiber length exceeds the order of 10^{16} m^{-2} [52], whereas the fibrin compositions described here are on the order of 10^{12} m^{-2} as seen in Fig. 4b and the void spaces between fibers are much larger than the 10 nm limit discussed in the work of Ogston et al..
4. The effective collision radius is equal to the sum of fiber and solute radii, which means that a collision is accounted for when there is simple contact between the two. This suggests that the fibers are impermeable, an assumption which is challenged for several of the studied compositions due to the large distances observed between individual protofibrils.

Assuming that fibers are permeable, the smaller solutes would be expected to diffuse through the fibers more easily than larger ones. This is confirmed in fig. 9 where the fitting curve for 10kDa dextran ($R^2 = 0.95$) shows a displacement to higher differences between predicted and experimental relative diffusivities as opposed to the curve of 40 kDa dextran ($R^2 = 0.84$), with an overall better fitting. Further, the protofibril distances in Fig. 9 represent approximate average values and not absolute gap sizes. The reason is that in fibers with lower numbers of protofibrils the original

crystalline structure is presumed to be maintained and gaps are formed because of void protofibril spaces and not because of a looser packing. Therefore, it is reasonable that a gradual increase is observed in the diffusivity differences relative to the protofibril distance of Fig. 9 instead of a certain cut-off threshold where the diffusing particles would either be small enough to penetrate or to collide with the fiber.

Furthermore, in order to assess whether fiber porosity is the main reason that the Ogston-predicted relative diffusivity deviates from the experimental values, further analysis was performed. This was done by adapting the fiber radius and the fiber volume fraction of different compositions to the values they would have if the fibers were non-porous, thus compensating for the void space within the fibers and the overestimation of the fiber volume fraction in the Ogston model. In such a hypothetical case, the fibers would exhibit the same network conformation but different fiber internal density, fiber radius and fiber volume fraction. Hence, assuming that the fibers are entirely impermeable, the fiber internal density would be equal to the fibrinogen density (ρ_{fib} = 1395 mg/mL) for all compositions, leaving no space between adjacent protofibrils. Since the protein mass would have to remain constant, the new fiber radii and fiber volume fractions were calculated accordingly, to compare the new set of Ogston-predicted values with those obtained experimentally. A comparison is demonstrated in Fig. S5. Errors are rather small for 10 kDa dextran with up to 7 and 5% difference for 20LH and 20HH compositions, respectively. This is expected, as in these conditions the porous fibers create more hindrance than the equivalent impermeable fibers. For 40 kDa dextran there is a good agreement for the compositions with low thrombin concentration and up to 9% difference for the compositions with high thrombin concentration. As discussed earlier, high thrombin concentrations cause faster cleaving of fibrinopeptides A and B of the fibrinogen molecule which results in a more violent formation of protofibrils and a faster polymerization. Therefore, under these conditions the protofibril voids within single fibers could be expected to spread more heterogeneously than in low-thrombin conditions, resulting in a greater variance of the protofibril distance estimated here. When the solute is small it can transfer through these voids freely, but when the solute reaches a critical size it could be temporarily entrapped, resulting in increased hindrance.

Having permeable fibers can be beneficial for biomedical applications in different ways. First, intrafibrous diffusion can help in reducing mass transport limitations in cell-encapsulated hydrogels and therefore promoting cell survival, which is important in tissue engineering [55]. If one interprets the difference between measured and predicted relative diffusivities in Fig. 9 as an estimate of the importance of intrafibrous diffusion, this effect is clearly becoming important for the high fibrinogen concentrations 20LH and 20HH, with a 76 and 64% difference relative to the predicted diffusivity of 10 kDa dextran, respectively. While measured diffusivities were the lowest for these compositions, their order of magnitude is still comparable to diffusivities measured for compositions with lower fibrinogen concentrations. Given the fact that diffusion distance is proportional to the square root of the diffusion coefficient, this leads to differences in diffusion distances of less than 8% (maximum difference found between 5HH and 20LH, for 10 kDa dextran). While one could speculate that such differences would not have a strong effect on cell survival in high versus low fibrinogen concentrations (at least not based on mass transport limitations), further experiments are needed to confirm this hypothesis. Secondly, therapeutic agents could be designed to penetrate individual fibrin fibers to induce fibrinolysis. At the same time, due to the affinity of several growth factors for fibrin [56], the voids within the fibers could provide additional binding sites for growth factors by increasing the area to volume ratio of the protein.

4.4 Changes in the molecular and network structure induce large differences in the shear modulus of fibrin hydrogels

Structural differences at the network and the individual fiber level are shown to induce large variations in the rheological response of the hydrogels, with G' values ranging over two orders of magnitude from 15 Pa (5HL) to 2283 Pa (20LL). There was up to a 20-fold increase of G' between compositions of 5 mg/mL fibrinogen and up to an 8-fold increase for 20 mg/mL fibrinogen. For all compositions, hydrogels with LL enzyme ratios exhibit the highest storage modulus, and those with HL ratios exhibit the lowest (Fig. 8d). LL ratios yield the fibers with the highest diameters (Fig. 5a) and lowest total fiber length, branch density and hydrogel fiber density among the same fibrinogen concentrations (Fig.

4b-d). Overall, the results obtained in this study are consistent with those reported in literature [20,23,57,58]. For the same enzyme ratios (LL, HL, LH, HH), higher fibrinogen concentrations consistently gave higher G' values. The effect of thrombin is not clear as contradictory findings have been reported in the literature; while a higher thrombin concentration decreased the material modulus in tensile tests of fibrin matrices encapsulating cells [58], a similar effect was only seen for higher thrombin to fibrinogen ratios (0.08 U/mg fibrinogen) in another study, with lower ratios having the opposite effect [20]. For the LH and HH compositions a different trend with thrombin concentration is seen for 5 and 20 mg/mL fibrinogen. However, 20LH and 20HH have a lower $CaCl_2$ concentration compared to 5LH and 5HH (4 mM versus 16 mM, see Table 1). This discrepancy in $CaCl_2$ concentration can also explain the larger relative increase for 20 mg/mL from LL to LH compared to 5 mg/mL, as stiffness has been reported to decrease in the presence of higher $CaCl_2$ concentrations [20].

The rheological response of fibrin hydrogels can be described in terms of their characteristics as semiflexible polymers, where individual fibers are treated as bundles of protofibrils of different densities that contribute to the overall stiffness in a nonlinear way, depending on how tight the fiber packing is. In this situation, the shear modulus would scale with the number of protofibrils as $G' \sim N_p^{7x/5}$, with x having values between 1 and 2 for loose (low N_p) and tight bundles (high N_p), respectively [34]. As shown in Fig. 5b, the number of protofibrils is highest for LL formulations which exhibit the highest storage moduli. The lowest values for number of protofibrils are seen for LH and HH especially for 20 mg/mL fibrinogen, where the stiffness values are relatively high, but presumably there is a trade-off between the effects of molecular structure (number of protofibrils) and network structure (fiber volume fraction).

Diffusivity is related to viscosity via the Stokes Einstein equation. At the same time, viscosity can be calculated from rheological measurements from the G''/ω ratio. This means that there is a link between relative diffusivity and rheological properties [59], within the linear viscoelastic region, when the time frame of the two properties is similar (i.e., at high frequency values in rheological experiments). However, no strong correlation was found between relative diffusivity and loss modulus in our data at the highest frequency (100 rad/s, fig. S6). This suggests that higher frequencies would be required to

probe the viscous response of the hydrogels in a time frame similar to that of the diffusivity experiments.

5. Conclusions

The structural and mechanical properties of fibrin hydrogels have been studied extensively [16,18,20,23,27,35], because of the importance of fibrin in blood coagulation and its potential in tissue engineering applications. However, so far, the relation between fibrin structure and diffusivity has not been studied extensively.

A novel combined methodological approach was used for the estimation of network and individual fiber properties relevant for fibrin clot mechanics and solute transport, from confocal fluorescence image stacks via the implementation of a fiber extraction algorithm, and turbidimetry. Turbidimetry has been extensively used for the quantification of individual fiber characteristics [19,23,35,60]; nevertheless, most studies have been performed with fibrin hydrogels at low fibrinogen concentrations (less than 2 mg/mL). On the other hand, fiber extraction algorithms have only recently been implemented for quantifying structural characteristics of fibrous networks [49,61–64]. In this study the two techniques were combined to yield complementary quantitative data, and at the same time this also allowed a comparison of the two methods in terms of total fiber length estimation, thus validating the results of turbidimetry for hydrogels of fibrinogen concentrations up to 20 mg/mL and at the same time showing the applicability and limitations of the fiber extraction algorithm for various compositions. Results from the fiber extraction algorithm for compositions which were poorly resolved such as 10LH, 10HH and 20HL should be treated with caution.

This quantitative structural analysis has shown that changes in fibrinogen, thrombin, factor XIII and calcium concentrations induce significant changes in the structure of the hydrogels, both in terms of the overall network organization and individual fiber characteristics. These variations only moderately affect the relative diffusivity of dextran solutes (25% difference between lowest and highest diffusivity

value for 40 kDa dextran). On the contrary, such changes in composition and structure have a large influence on the linear viscoelastic properties of the hydrogels (two orders of magnitude difference between lowest and highest modulus value). Finally, a combined structural and diffusional analysis provided evidence that loosely packed fibrin fibers are permeable to small solutes and this permeability is dependent on the average distance between individual protofibrils.

The structural, diffusional and mechanical characteristics of ECM substitutes are of crucial importance in tissue engineering, as they affect cell fate. Our findings support the potential of fibrin hydrogels in this context, as they can be tailored to the needs of a specific application simply by changing the concentrations of individual constituents. As discussed earlier, the fact that fibrin fibers can be permeable to solute transport may help in reducing mass transport limitations and promote cell survival. Further, fibrin is known for its ability to bind growth factors via its heparin-binding domains [56]. This, again in combination with the semi-permeability of fibrin fibers shown in this study, can prove to be a promising feature because it would allow the entrapment of growth factors within individual fibers and the formation of growth factor gradients by using hydrogel layers of different fiber densities in an ECM substitute. As this study merely concerns materials characterization, one can only speculate at this stage on how our findings would affect the quest for an optimal fibrin hydrogel carrier for a specific application in tissue engineering. Based on our diffusion measurements, no substantial differences in mass transport limitations or cell survival due to these limitations are expected for the different compositions tested. This is even the case for the high fibrinogen concentrations (20 mg/mL), for which intrafibrous diffusion may be an important contributor to mass transport (in particular for the 20LH and 20HH compositions). As our data demonstrates a strong effect of composition on structural and mechanical (bulk rheological) properties, these may be more important to consider for the optimization of fibrin hydrogels for a specific application. Measured storage moduli covered two orders of magnitude within a range that is known to affect cell behavior in terms of differentiation [10,65], and also independently from the material porosity [66]. Low fibrinogen concentrations with relatively low thrombin and factor XIII concentrations (such as 5LL here) exhibited a much more open porous structure and therefore less confinement to cells. This may

facilitate spreading and proliferation of encapsulated cells in 3D [67]. Again, it is worth noting that these are merely speculations, also because cell encapsulation may lead to modification of the fiber network structure, and the optimal properties of the carrier material can drastically change, depending on the cell type and the specific application. Additional experiments will be needed to address these aspects.

Tables

Table 1: Final fibrin hydrogel compositions used in this study. Structural and diffusional characterization was performed on all 12 compositions. Mechanical characterization was performed on 8 compositions (5 and 20 mg/mL fibrinogen concentrations). Letters at the top refer to (relative) thrombin (first letter) and factor XIII (second letter) concentrations (L=Low, H=High).

	LL			**HL**			**LH**			**HH**		
Fibrinogen (mg/mL)	5	10	20	5	10	20	5	10	20	5	10	20
Thrombin (U/mg fibrinogen)	0.02			0.2			0.02			0.2		
Factor XIII (U/mg fibrinogen)	0.02			0.02			2			2		
Ionic strength (mM)	210	210	210	210	210	210	208	206	201	208	206	201
$CaCl_2$ (mM)	20	20	20	20	20	20	16	12	4	16	12	4

Table 2: Fibrin hydrogel network properties. Symbols in parentheses are referred to in 'Turbidimetry' section.

Property	**Units**	**Quantification method**
Total fiber length (ρ_L)	Total fiber length/Hydrogel volume (μm^{-2})	Fiber extraction algorithm
Hydrogel fiber density	Number of fibers/Hydrogel volume (μm^{-3})	Fiber extraction algorithm
Fiber volume fraction (Φ)	Total fiber volume/Hydrogel volume	Turbidimetry
Branch density	Total number of branches/Hydrogel volume (μm^{-3})	Fiber extraction algorithm

Fiber connectivity	Number of fibers/Number of branches	Fiber extraction algorithm

Table 3: Individual fiber properties

Property	**Units**	**Quantification method**
Fiber radius (r_f)	nm	Turbidimetry
Average fiber length	Total length of the fibers/Number of fibers (μm)	Fiber extraction algorithm
Number of protofibrils (N_p)	Number of protofibrils/fiber cross section	Turbidimetry
Fiber internal density (ρ_f)	Protein mass/fiber volume (mg/mL)	Turbidimetry
Protofibril distance (d_{pf})	nm	Turbidimetry

Figure captions

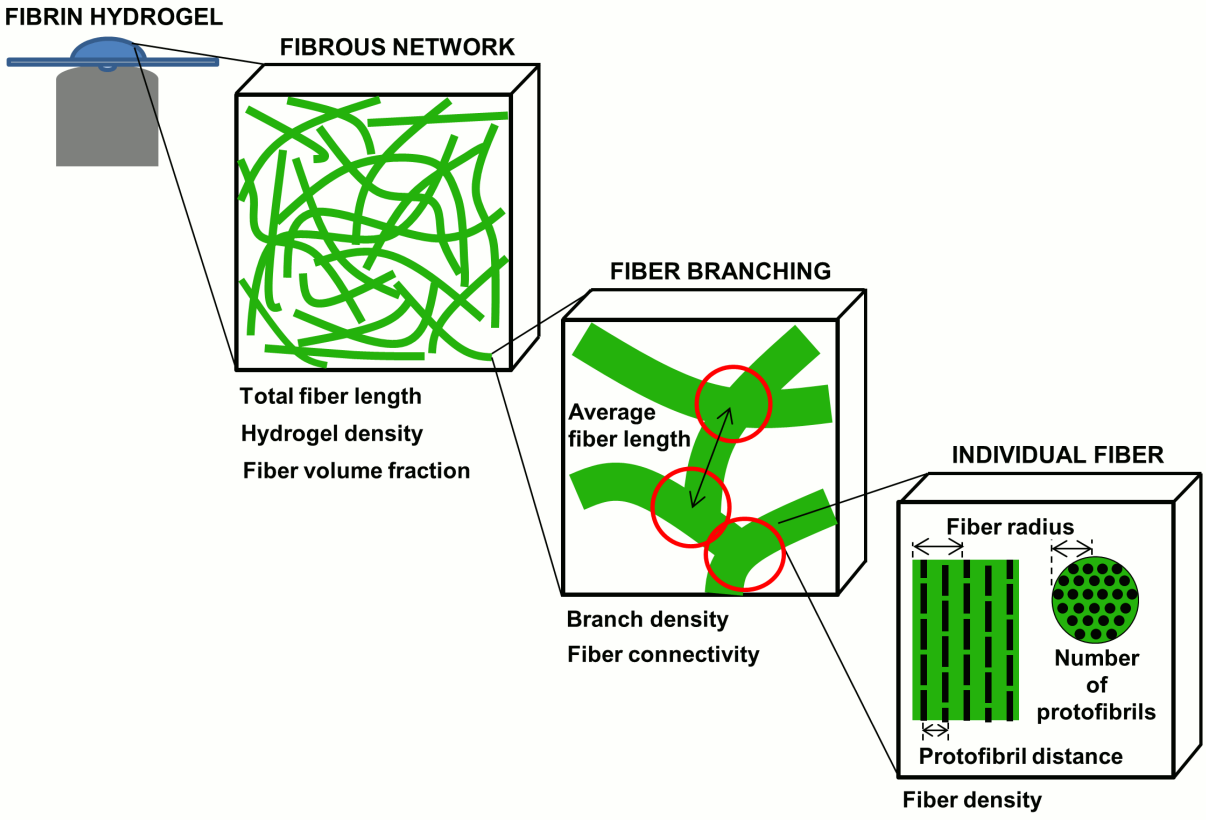

Fig. 1: Structural parameters for individual fiber and network properties of fibrin hydrogels. Parameters are further explained in Tables 2 and 3.

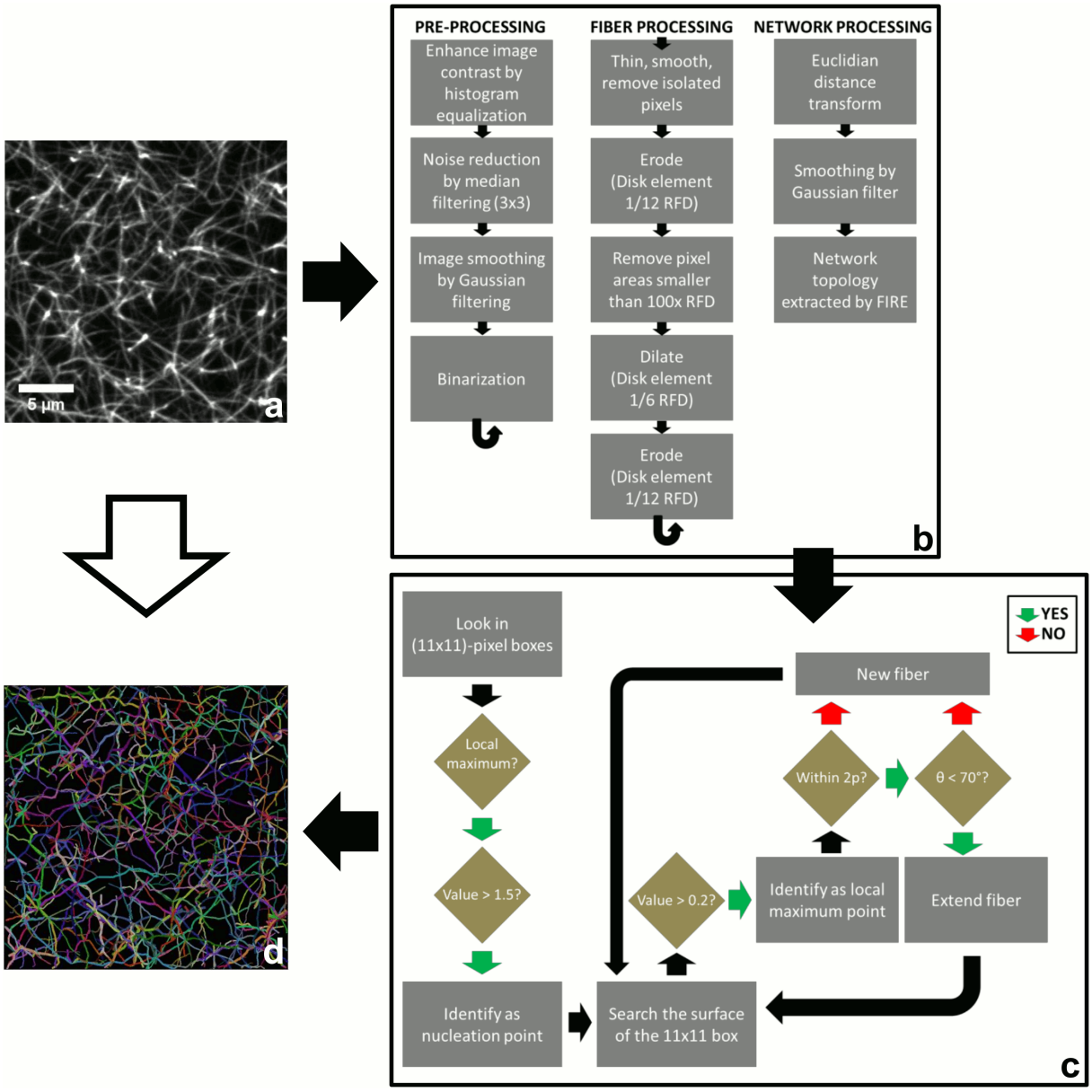

Fig. 2: Image stacks acquired with confocal microscopy (a) were submitted to multiple processing steps (RFD is the representative fiber diameter) (b) for an optimal depiction of the fibers before the FIRE algorithm [49] *was implemented (c) to result in an accurate depiction of the network (d) Pseudocolors depict individual fibers.*

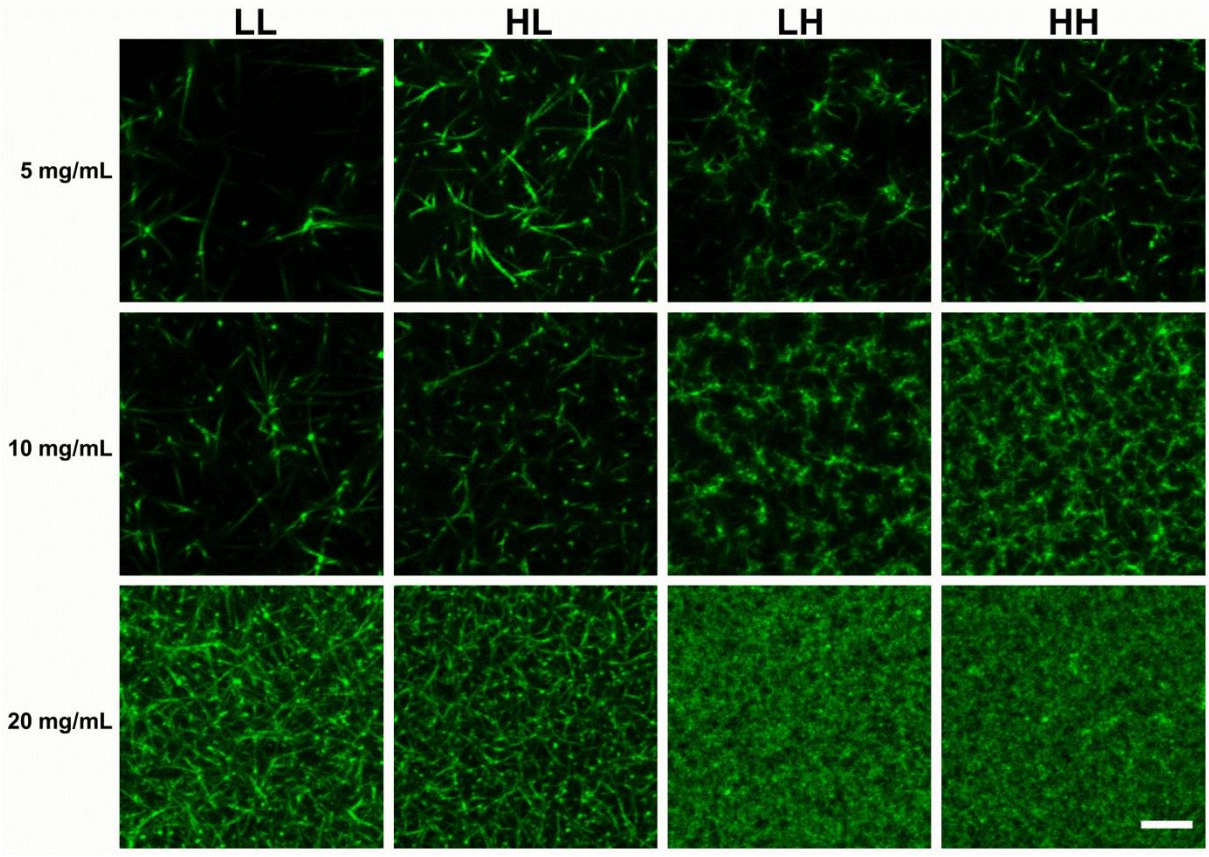

Fig.3: Confocal images of the fibrous micro-structure of fibrin. Numbers on the left side refer to fibrinogen concentration. Letters at the top refer to (relative) thrombin (first letter) and factor XIII (second letter) concentrations (L=Low, H=High; for corresponding values see Table 1). Scale bar is 5 μm.

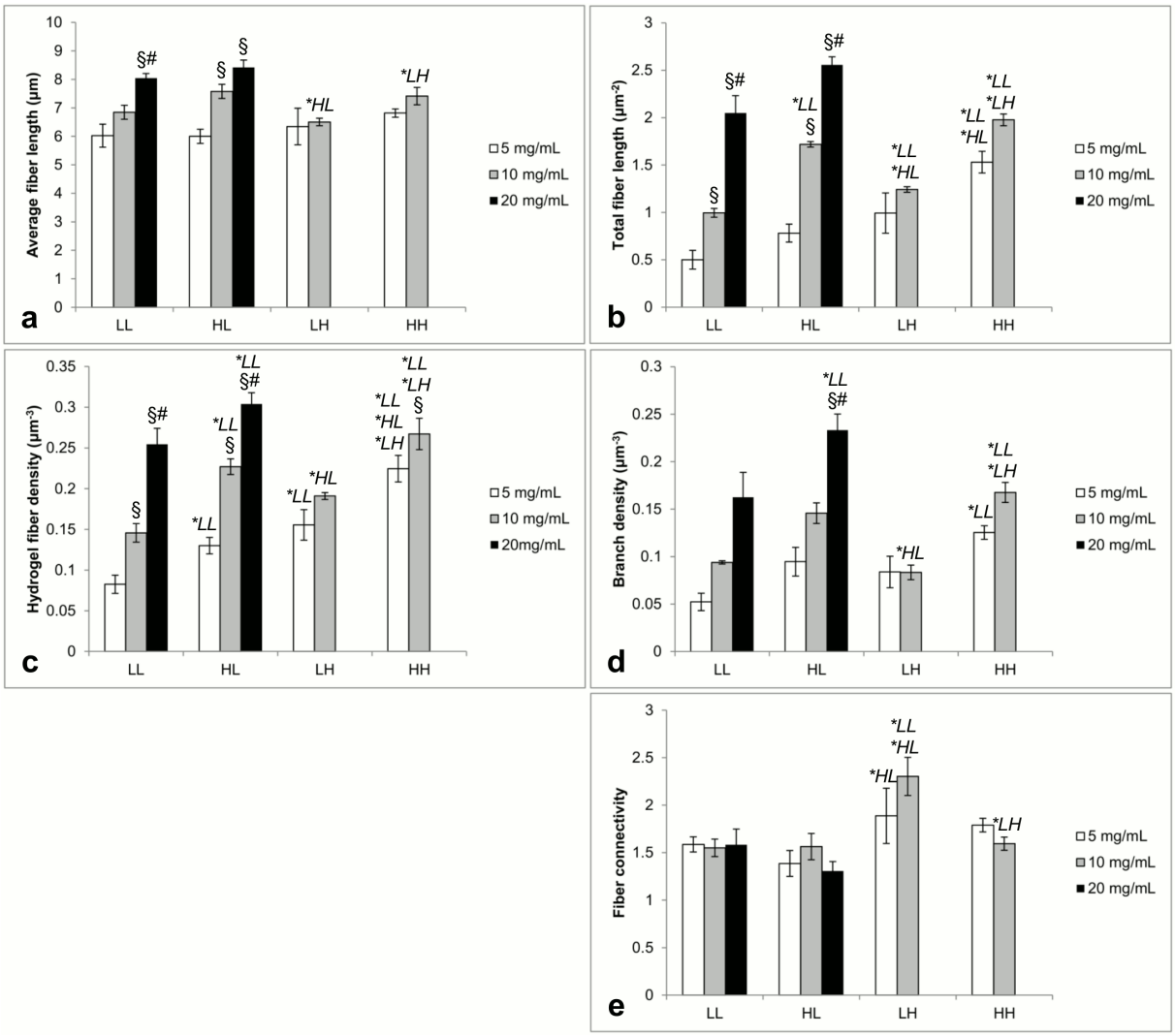

*Fig. 4: Network and individual fiber characteristics determined by the fiber extraction algorithm for different fibrinogen concentrations (5, 10, 20 mg/mL) and thrombin and factor XIII concentrations (LL, HL, LH, HH; see Table 1). Symbols § and # denote significant differences with 5 and 10 mg/mL of the same enzyme concentration, respectively. * followed by a specific enzyme composition denotes significant differences with the specific enzyme composition of the same fibrinogen concentration ($p<0.05$). Error bars represent standard deviations.*

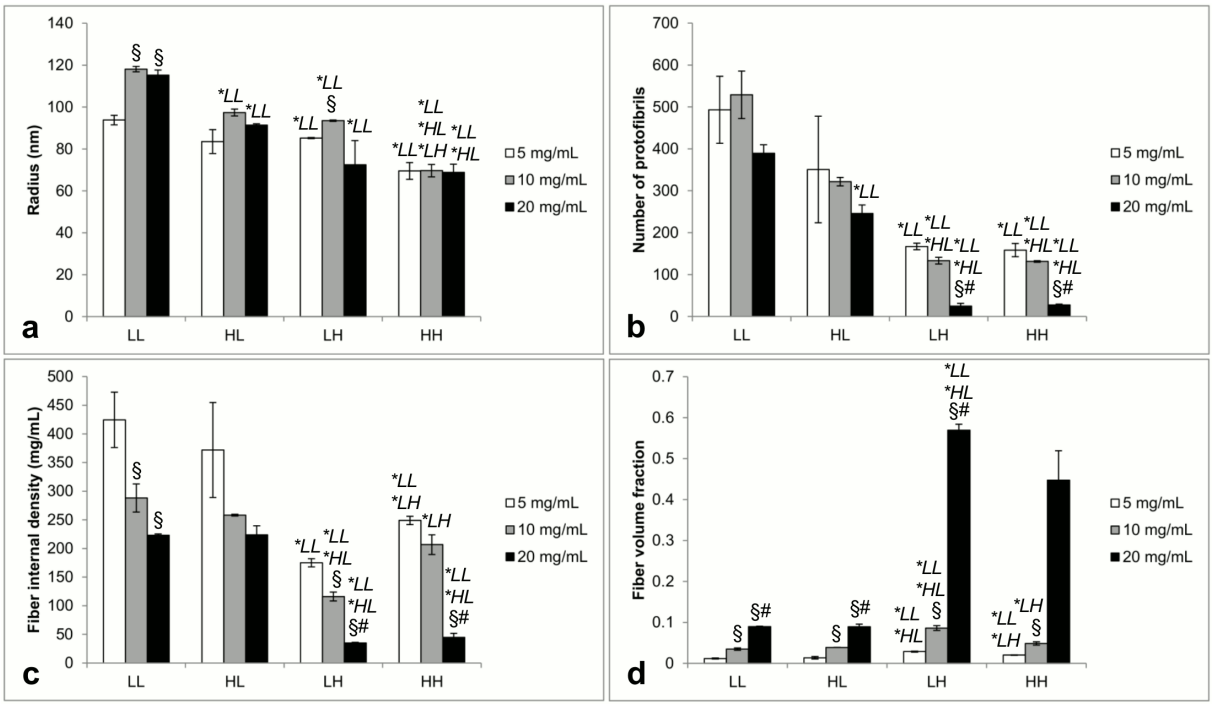

*Fig. 5: Fibrin hydrogel structural characteristics and average fiber properties determined from turbidimetry for different fibrinogen concentrations (5, 10, 20 mg/mL) and thrombin and factor XIII concentrations (LL, HL, LH, HH; see Table 1) Symbols § and # denote significant differences with 5 or 10 mg/mL of the same enzyme concentration, respectively. * followed by a specific enzyme composition denotes significant differences with the specific enzyme composition of the same fibrinogen concentration ($p<0.05$). Error bars represent standard deviations.*

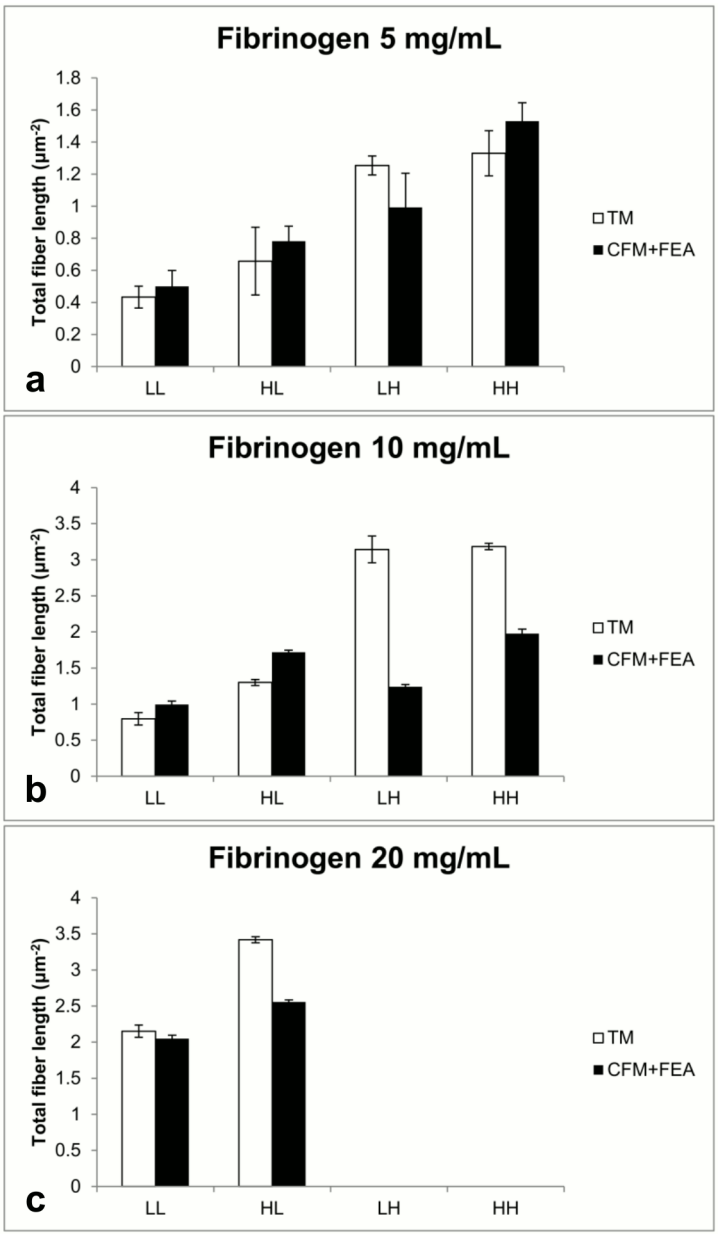

Fig 6: Comparison of total fiber length as determined independently from turbidimetry (TM) and confocal fluorescence microscopy with the fiber extraction algorithm (CFM+FEA) for different fibrinogen (5, 10 and 20 mg/mL) thrombin and factor XIII concentrations (LL, HL, LH, HH; see Table 1 for more details).

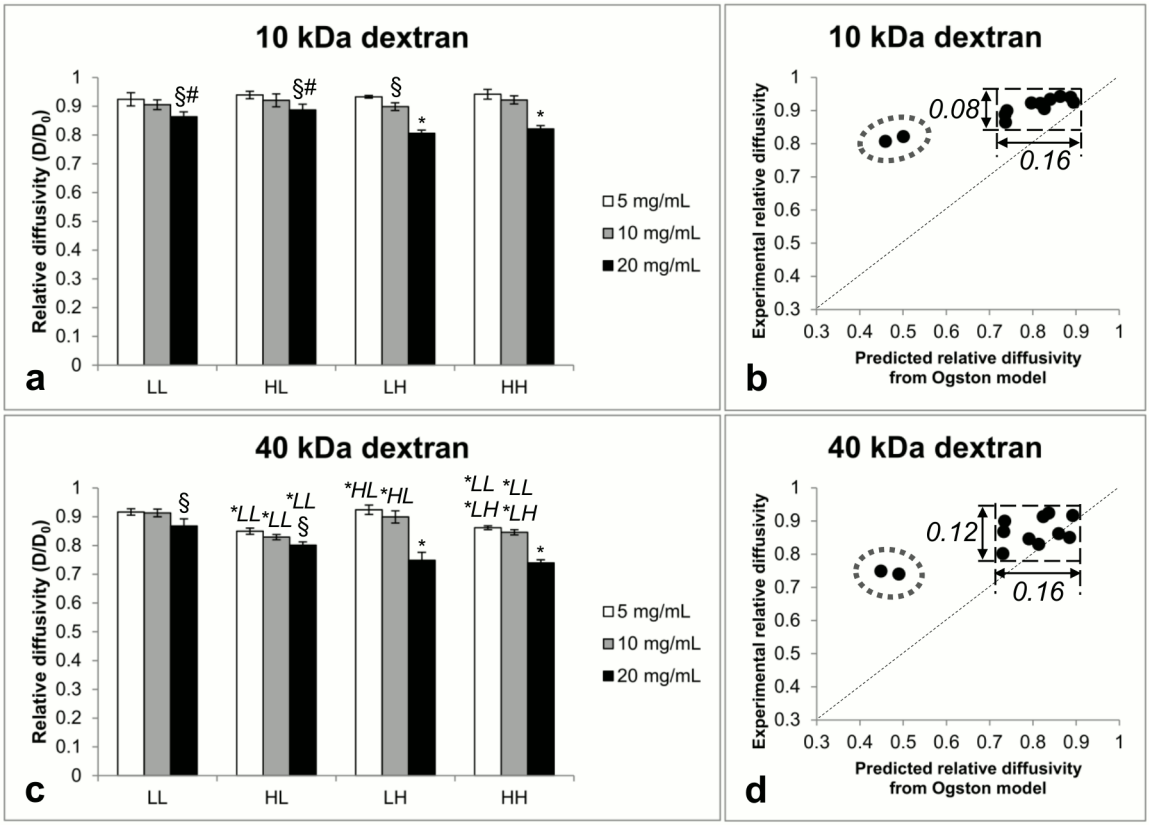

*Fig. 7: Relative diffusivities of 10 kDa (a) and 40 kDa (c) dextran in fibrin hydrogels of different fibrinogen (5, 10 and 20 mg/mL) thrombin and factor XIII concentrations (LL, HL, LH, HH; see Table 1 for more details). Symbols § and # denote significant differences with 5 or 10 mg/mL of the same enzyme concentration, respectively. * followed by a specific enzyme composition denotes significant differences with the specific enzyme composition of the same fibrinogen concentration and with all other compositions for LH and HH in (a) ($p<0.05$). Error bars represent standard deviations. (b) and (d): Comparison of diffusivity values obtained by FRAP experiments and estimated by the Ogston model. The encircled data points represent the 20LH and 20HH compositions. Bounding boxes around the other data points indicate the data range for predicted and experimental values of all other compositions. Dashed line has slope 1 (equal experimental and predicted values).*

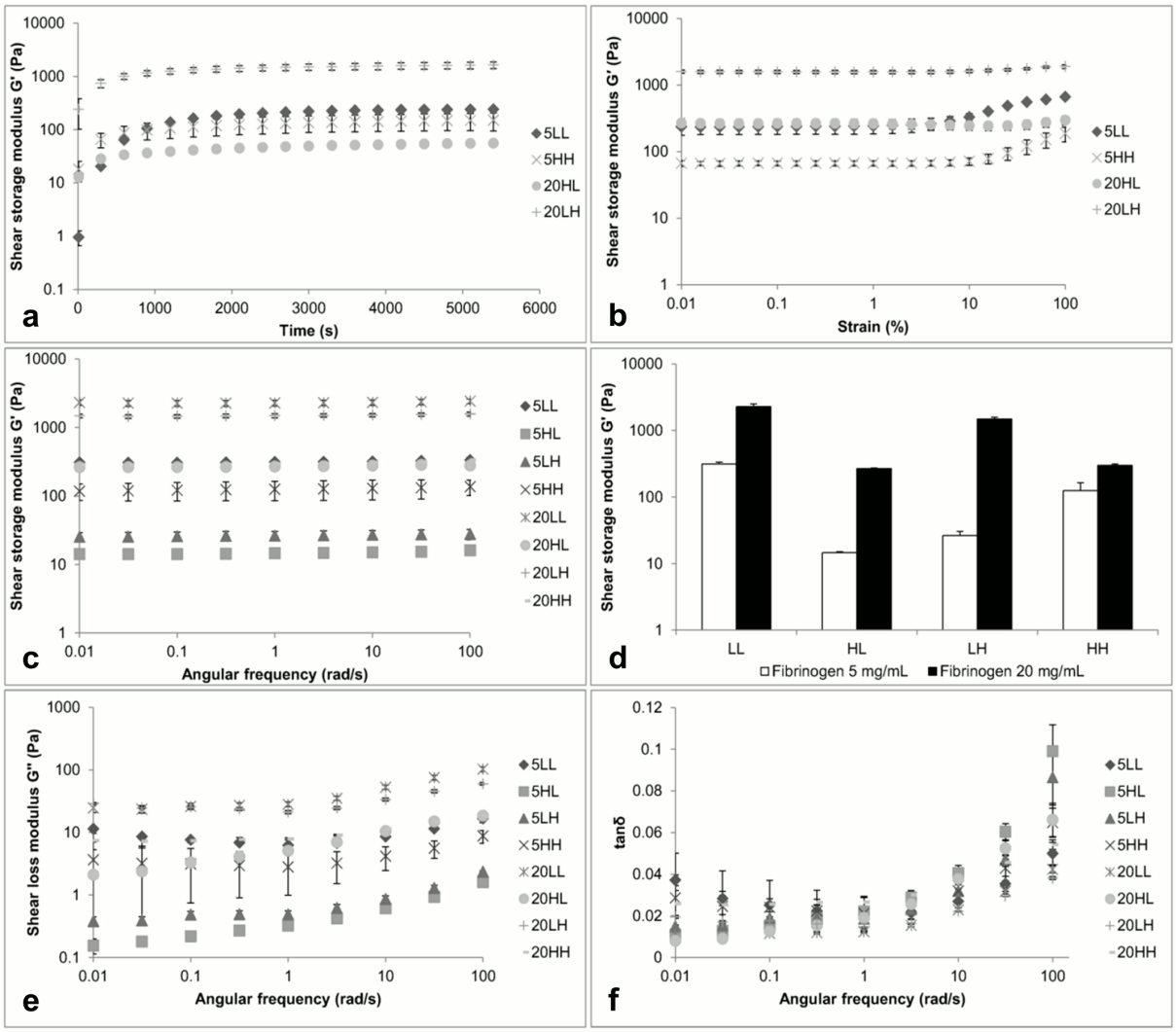

Fig. 8: Rheological characterization of fibrin hydrogels. (a) Curves of G′ versus time at γ = 1% and ω = 1 rad/s, (b) post-polymerization strain-sweep curves at ω= 1 rad/s for the estimation of LVE region, (c) frequency-sweep curves for γ=1%, (d) G′ values averaged from the frequency-sweep measurements at ω=1 rad/s and γ=1%, (e) loss modulus G″ from the frequency-sweep measurements and (f) tanδ=G″/G′ values from the frequency-sweep tests. Error bars represent standard deviations.

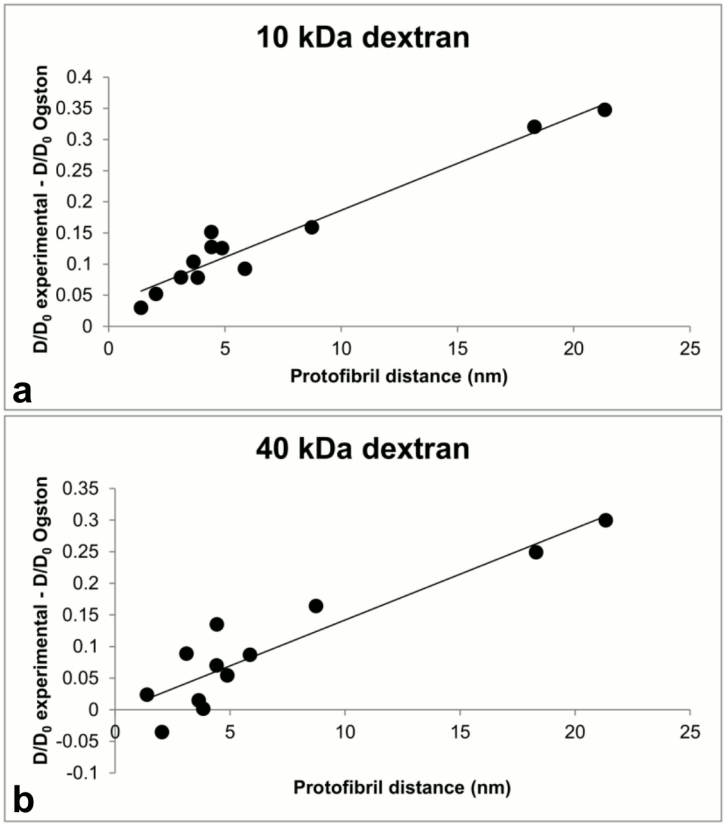

Fig. 9: Differences between experimental and predicted values of relative diffusivity versus the end-to-end distance of individual protofibrils. R^2= 0.95 for the linear fit for 10 kDa (a) and R^2= 0.84 for 40 kDa dextran (b).

Acknowledgements

The research leading to these results has received funding from the European Research Council under the European Union's Seventh Framework Programme (FP7/2007-2013)/ ERC Grant Agreement n° 308223) and from the Research Foundation-Flanders (FWO – project number G.0858.12). DL gratefully acknowledges funding from the Research Fund KU Leuven (PDMK/14/203) and from the Research Foundation Flanders (FWO – grant number 12I6216N). GK and BV acknowledge the Foundation for Fundamental Research on Matter (FOM), which is part of the Netherlands Organization for Scientific Research (NWO), for funding. Professor Hideaki Mizuno is acknowledged for providing lab space and equipment for part of this work. This work is part of Prometheus, the Leuven R&D Division of Skeletal Tissue Engineering of the KU Leuven.

References

1. Censi R, Di Martino P, Vermonden T, Hennink WE (2012) Hydrogels for protein delivery in tissue engineering. *J Control release* **161**: 680–692.

2. Drury JL, Mooney DJ (2003) Hydrogels for tissue engineering: scaffold design variables and applications. *Biomaterials* **24**: 4337–4351.

3. Raeber GP, Lutolf MP, Hubbell J a (2005) Molecularly engineered PEG hydrogels: a novel model system for proteolytically mediated cell migration. *Biophys J* **89**: 1374–1388.

4. Moreira Teixeira LS, Feijen J, van Blitterswijk CA, Dijkstra PJ, Karperien M (2012) Enzyme-catalyzed crosslinkable hydrogels: emerging strategies for tissue engineering. *Biomaterials* **33**: 1281–1290.

5. Vats K, Benoit DS (2013) Dynamic Manipulation of Hydrogels to Control Cell Behavior : A Review. *Tissue Eng Part B* **19**: 455–469.

6. Stevens MM, George JH (2005) Exploring and engineering the cell surface interface. *Science* **310**: 1135–1138.

7. Discher DE, Janmey P, Wang Y-L (2005) Tissue cells feel and respond to the stiffness of their substrate. *Science* **310**: 1139–1143.

8. Yeung T, Georges PC, Flanagan LA, Marg B, Ortiz M, Funaki M, Zahir N, Ming W, Weaver V, Janmey PA (2005) Effects of substrate stiffness on cell morphology, cytoskeletal structure, and adhesion. *Cell Motil Cytoskeleton* **60**: 24–34.

9. Lo CM, Wang HB, Dembo M, Wang YL (2000) Cell movement is guided by the rigidity of the substrate. *Biophys J* **79**: 144–152.

10. Engler AJ, Sen S, Sweeney HL, Discher DE (2006) Matrix elasticity directs stem cell lineage

specification. *Cell* **126**: 677–689.

11. Nelson CM, Jean RP, Tan JL, Liu WF, Sniadecki NJ, Spector A a, Chen CS (2005) Emergent patterns of growth controlled by multicellular form and mechanics. *Proc Natl Acad Sci U S A* **102**: 11594–11599.

12. Swartz MA, Fleury ME (2007) Interstitial Flow and Its Effects in Soft Tissues. *Annu Rev Biomed Eng* **9**: 229–256.

13. Brandl F, Kastner F, Gschwind RM, Blunk T, Tessmar J, Göpferich A (2010) Hydrogel-based drug delivery systems: comparison of drug diffusivity and release kinetics. *J Control Release* **142**: 221–228.

14. Ahmed TAE, Dare E V, Hincke M (2008) Fibrin: A Versatile Scaffold for Tissue Engineering Applications. *Tissue Eng Part B Rev* **14**: 199–215.

15. Wolberg AS (2007) Thrombin generation and fibrin clot structure. *Blood Rev* **21**: 131–142.

16. Ferri F, Greco M, Arcovito G, Bassi F, De Spirito M, Paganini E, Rocco M (2001) Growth kinetics and structure of fibrin gels. *Phys Rev E* **63**: 31401.

17. De Spirito M, Arcovito G, Papi M, Rocco M, Ferri F (2003) Small and wide angle elastic light scattering study of fibrin structure. *J Appl Crystallogr* **36**: 636–641.

18. Yeromonahos C, Polack B, Caton F (2010) Nanostructure of the fibrin clot. *Biophys J* **99**: 2018–2027.

19. Ferri F, Calegari GR, Molteni M, Cardinali B, Magatti D, Rocco M (2015) Size and Density of Fibers in Fibrin and Other Filamentous Networks from Turbidimetry: Beyond a Revisited Carr–Hermans Method, Accounting for Fractality and Porosity. *Macromolecules* **48**: 5423–5432.

20. Ryan EA, Mockros LF, Weisel JW, Lorand L (1999) Structural Origins of Fibrin Clot Rheology. *Biophys J* **77**: 2813–2826.

21. Carr ME, Gabriel D a, McDonagh J (1986) Influence of Ca2+ on the structure of reptilase-derived and thrombin-derived fibrin gels. *Biochem J* **239**: 513–516.

22. Di Stasio E, Nagaswami C, Weisel JW, Di Cera E (1998) Cl- regulates the structure of the fibrin clot. *Biophys J* **75**: 1973–1979.

23. Kurniawan NA, Grimbergen J, Koopman J, Koenderink GH (2014) Factor XIII stiffens fibrin clots by causing fiber compaction. *J Thromb Haemost* **12**: 1687–1696.

24. Spero RC, Sircar RK, Schubert R, Taylor RM, Wolberg AS, Superfine R (2011) Nanoparticle diffusion measures bulk clot permeability. *Biophys J* **101**: 943–950.

25. Kim O V, Xu Z, Rosen ED, Alber MS (2013) Fibrin networks regulate protein transport during thrombus development. *PLoS Comput Biol* **9**: e1003095.

26. Wufsus AR, Macera NE, Neeves KB (2013) The hydraulic permeability of blood clots as a function of fibrin and platelet density. *Biophys J* **104**: 1812–1823.

27. Weigandt KM, Pozzo DC, Porcar L (2009) Structure of high density fibrin networks probed with neutron scattering and rheology. *Soft Matter* **5**: 4321.

28. Voter WA, Lucaveche C, Erickson HP (1986) Concentration of protein in fibrin fibers and fibrinogen polymers determined by refractive index matching. *Biopolymers* **25**: 2375–2384.

29. Baradet TC, Haselgrove JC, Weisel JW (1995) Three-dimensional reconstruction of fibrin clot networks from stereoscopic intermediate voltage electron microscope images and analysis of branching. *Biophys J* **68**: 1551–1560.

30. Carr ME, Hermans J (1978) Size and density of fibrin fibers from turbidity. *Macromolecules* **11**: 46–50.

31. Molteni M, Magatti D, Cardinali B, Rocco M, Ferri F (2013) Fast two-dimensional bubble analysis of biopolymer filamentous networks pore size from confocal microscopy thin data stacks. *Biophys J* **104**: 1160–1169.

32. Münster S, Fabry B (2013) A Simplified Implementation of the Bubble Analysis of Biopolymer Network Pores. *Biophys J* **104**: 2774–2775.

33. Paesen R, Sanen K, Smisdom N, Michiels L, Ameloot M (2014) Polarization second harmonic generation by image correlation spectroscopy on collagen type i hydrogels. *Acta Biomater* **10**: 2036–2042.

34. Piechocka IK, Jansen KA, Broedersz CP, Kurniawan NA, MacKintosh FC, Koenderink GH (2016) Multi-scale strain-stiffening of semiflexible bundle networks. *Soft Matter* **12**: 2145–2156.

35. Piechocka IK, Bacabac RG, Potters M, Mackintosh FC, Koenderink GH (2010) Structural hierarchy governs fibrin gel mechanics (Supporting Material). *Biophys J* **98**: 2281–2289.

36. MacKintosh FC, Kas J, Janmey PA (1995) Elasticity of semiflexible biopolymer networks. *Phys Rev Lett* **75**: 4425–4428.

37. Wufsus AR, Rana K, Brown A, Dorgan JR, Liberatore MW, Neeves KB (2015) Elastic behavior and platelet retraction in low- and high-density fibrin gels. *Biophys J* **108**: 173–183.

38. Brown AEX, Litvinov RI, Discher DE, Purohit PK, Weisel JW (2009) Multiscale mechanics of fibrin polymer: gel stretching with protein unfolding and loss of water. *Science* **325**: 741–744.

39. Shkilnyy A, Proulx P, Sharp J, Lepage M, Vermette P (2012) Diffusion of rhodamine B and bovine serum albumin in fibrin gels seeded with primary endothelial cells. *Colloids Surf B Biointerfaces* **93**: 202–207.

40. Adhikari AS, Mekhdjian AH, Dunn AR (2012) Strain tunes proteolytic degradation and diffusive transport in fibrin networks. *Biomacromolecules* **13**: 499–506.

41. Nauman J V, Campbell PG, Lanni F, Anderson JL (2007) Diffusion of insulin-like growth factor-I and ribonuclease through fibrin gels. *Biophys J* **92**: 4444–4450.

42. Chiu CL, Hecht V, Duong H, Wu B, Tawil B (2012) Permeability of three-dimensional fibrin

constructs corresponds to fibrinogen and thrombin concentrations. *Biores Open Access* **1**: 34–40.

43. De Spirito M, Missori M, Maulucci G, Teixeira J, Papi M (2011) Nanocavities trapped along fibrin fibers allow the diffusion of thrombolytic drugs. *Appl Phys Lett* **99**: 223701.

44. Yang Z, Mochalkin I, Doolittle RF (2000) A model of fibrin formation based on crystal structures of fibrinogen and fibrin fragments complexed with synthetic peptides. *Proc Natl Acad Sci U S A* **97**: 14156–14161.

45. Ekani-Nkodo A, Fygenson DK (2003) Size exclusion and diffusion of fluoresceinated probes within collagen fibrils. *Phys Rev E Stat Nonlin Soft Matter Phys* **67**: 21909.

46. Yao L, Swartz DD, Gugino SF, Russell J a, Andreadis ST (2005) Fibrin-based tissue-engineered blood vessels: differential effects of biomaterial and culture parameters on mechanical strength and vascular reactivity. *Tissue Eng* **11**: 991–1003.

47. Eyrich D, Brandl F, Appel B, Wiese H, Maier G, Wenzel M, Staudenmaier R, Goepferich A, Blunk T (2007) Long-term stable fibrin gels for cartilage engineering. *Biomaterials* **28**: 55–65.

48. Willerth SM, Arendas KJ, Gottlieb DI, Sakiyama-Elbert SE (2006) Optimization of fibrin scaffolds for differentiation of murine embryonic stem cells into neural lineage cells. *Biomaterials* **27**: 5990–6003.

49. Stein AM, Vader DA, Jawerth LM, Weitz DA, Sander LM (2008) An algorithm for extracting the network geometry of three-dimensional collagen gels. *J Microsc* **232**: 463–475.

50. Lambrechts D, Roeffaers M, Goossens K, Hofkens J, Van de Putte T, Schrooten J, Van Oosterwyck H (2014) A causal relation between bioluminescence and oxygen to quantify the cell niche. *PLoS One* **9**: e97572.

51. Jönsson P, Jonsson MP, Tegenfeldt JO, Höök F (2008) A method improving the accuracy of fluorescence recovery after photobleaching analysis. *Biophys J* **95**: 5334–5348.

52. Ogston AG, Preston BN, Wells JD (1973) On the Transport of Compact Particles Through Solutions of Chain-Polymers. *Proc R Soc A Math Phys Eng Sci* **333**: 297–316.

53. Weisel JW, Nagaswami C (1992) Computer modeling of fibrin polymerization kinetics correlated with electron microscope and turbidity observations: clot structure and assembly are kinetically controlled. *Biophys J* **63**: 111–128.

54. Weisel JW (2004) The mechanical properties of fibrin for basic scientists and clinicians. *Biophys Chem* **112**: 267–276.

55. Demol J, Lambrechts D, Geris L, Schrooten J, Van Oosterwyck H (2011) Towards a quantitative understanding of oxygen tension and cell density evolution in fibrin hydrogels. *Biomaterials* **32**: 107–118.

56. Martino MM, Briquez PS, Ranga A, Lutolf MP, Hubbell JA (2013) Heparin-binding domain of fibrin(ogen) binds growth factors and promotes tissue repair when incorporated within a synthetic matrix. *Proc Natl Acad Sci U S A* **110**: 4563–4568.

57. Moreno-Arotzena O, Mendoza G, Cóndor M, Rüberg T, JM G-A (2014) Inducing chemotactic and haptotactic cues in microfluidic devices for three- dimensional in vitro assays Inducing chemotactic and haptotactic cues in microfluidic devices for three-dimensional in vitro assays. *Biomicrofluidics* **8**: 64122.

58. Rowe SL, Lee S, Stegemann JP (2007) Influence of thrombin concentration on the mechanical and morphological properties of cell-seeded fibrin hydrogels. *Acta Biomater* **3**: 59–67.

59. Mason TG (2000) Estimating the viscoelastic moduli of complex fluids using the generalized Stokes-Einstein equation. *Rheol Acta* **39**: 371–378.

60. Carr ME, Shen LL, Hermans J (1977) Mass-length ratio of fibrin fibers from gel permeation and light scattering. *Biopolymers* **16**: 1–15.

61. Chen J, Kim O V., Litvinov RI, Weisel JW, Alber MS, Chen DZ (2014) An automated

approach for fibrin network segmentation and structure identification in 3D confocal microscopy images. *Proc - IEEE Symp Comput Med Syst* 173–178.

62. Kim E, Kim O V, Machlus KR, Liu X, Kupaev T, Lioi J, Wolberg AS, Chen DZ, Rosen ED, Xu Z, et al. (2011) Correlation between fibrin network structure and mechanical properties: an experimental and computational analysis. *Soft Matter* **7**: 4983.

63. D'Amore A, Stella J a, Wagner WR, Sacks MS (2010) Characterization of the complete fiber network topology of planar fibrous tissues and scaffolds. *Biomaterials* **31**: 5345–5354.

64. Xu T, Vavylonis D, Tsai F-C, Koenderink GH, Nie W, Yusuf E, Lee I-J, Wu J-Q, Huang X (2015) SOAX: a software for quantification of 3D biopolymer networks. *Sci Rep* **5**: 9081.

65. Mao AS, Shin J-W, Mooney DJ (2016) Effects of substrate stiffness and cell-cell contact on mesenchymal stem cell differentiation. *Biomaterials* **98**: 184–191.

66. Wen JH, Vincent LG, Fuhrmann A, Choi YS, Hribar KC, Taylor-Weiner H, Chen S, Engler AJ (2014) Interplay of matrix stiffness and protein tethering in stem cell differentiation. *Nat Mater* **13**: 979–987.

67. Catelas I, Ph D, Sese N, Wu BM, Dunn JCY, Helgerson SAM, Tawil B (2006) Human Mesenchymal Stem Cell Proliferation and Osteogenic Differentiation in Fibrin Gels in Vitro. *Tissue Eng* **12**: 2385–2396.

68. Mischenko M, Travis L, Lacis A (2002) Scattering, absorption, and emission of light by small particles. *NASA Goddard Inst Sp Stud New York Inst Sp Stud New York pace Stud New York New York* 1–128.

Supporting Material

A. Structural characterization of the fibrin network

Fiber Extraction Algorithm

Image stacks of the fibrin network were loaded in MATLAB (The MathWorks, Natick, MA) and processed using custom-made image analysis algorithms. Pre-processing of the image stacks was performed in accordance with the approach described by D'Amore et al. [63]. Image contrast was enhanced via a histogram equalization algorithm (histeq function in MATLAB) and noise on the images was reduced by a 3 by 3 median filtering operation (medfilt2 function in MATLAB). Images were subsequently smoothed with a Gaussian filter (with a standard deviation of 1 pixel) and binarized by keeping a percentage of the maximal pixel intensities. These percentages were carefully chosen to obtain a good qualitative match between the original and binarized fiber network for the various hydrogel formulations, which was always the lowest possible value for the best representation without having a disrupted extracted fiber network. Fiber areas in the binarized images were then thinned and smoothed, and isolated pixels were removed using the bwmorph MATLAB function (with 'thin', 'majority', and 'clean' option, respectively). Fibers were refined via an image erosion operation on the binarized images (imerode function in MATLAB, using a disk element with size 1/12 of a representative fiber diameter, RFD). Estimations for RFD were obtained from Wufsus et al. [26], describing an average fiber radius of ~60 nm, which equals a size of 0.6 pixel. Pixel areas smaller than 100xRFD were removed via the bwareaopen function in MATLAB. Binarized fiber areas were dilated (via the imdilate MATLAB function with disk element size of RFD/6) and eroded again (imerode function with a disk size element of RFD/12).

The distance from a pixel contained in the fiber area to the nearest background pixel was calculated via a Euclidian distance transform on the binarized image stack. The 2D images contained in the image stack have an isotropic pixel aspect ratio and could be transformed via the bwdist MATLAB function. Along the z axis, an anisotropic voxel aspect ratio was present and therefore required the use

of a line-scan algorithm to calculate the Euclidian distance transform [68]. The distance transform was smoothed with a Gaussian filter with standard deviation of 0.2 pixels.

Network topology was extracted with the fiber extraction (FIRE) algorithm described by Stein et al [49]. In brief, nucleation points were identified at local maxima of the distance transform (points were traced in a surrounding box with size of 11 by 11 pixels) that also exceeded a threshold value of 1.5 pixels. Next, local maximum points (LMPs) were searched on the surface of the surrounding box and were identified as local maxima when larger than a threshold value of 0.2. Extensions of nucleation points to these LMPs were defined as new fiber branches and were extended until they reached an end position. End positions of a fiber were reached at other nucleation points or if no new LMPs could be identified. New LMPs were obtained if a minimal distance of 2 pixels lay between 2 LMPs and if changes in fiber direction resulting from fiber extension were not larger than 70°. Identified fibers were removed when they were shorter than 15 pixels and had a minimal difference in angle of 10° with another fiber going through the same nucleation point. Fibers that had a similar orientation at the end were linked together to form a single fiber. Fiber ends that were separated by 25 pixels and had a minimum angle of 130° between them were connected to make a single fiber. The total fiber length in each composition was quantified from the extracted network by summation of all individual fiber segment lengths.

Turbidimetry

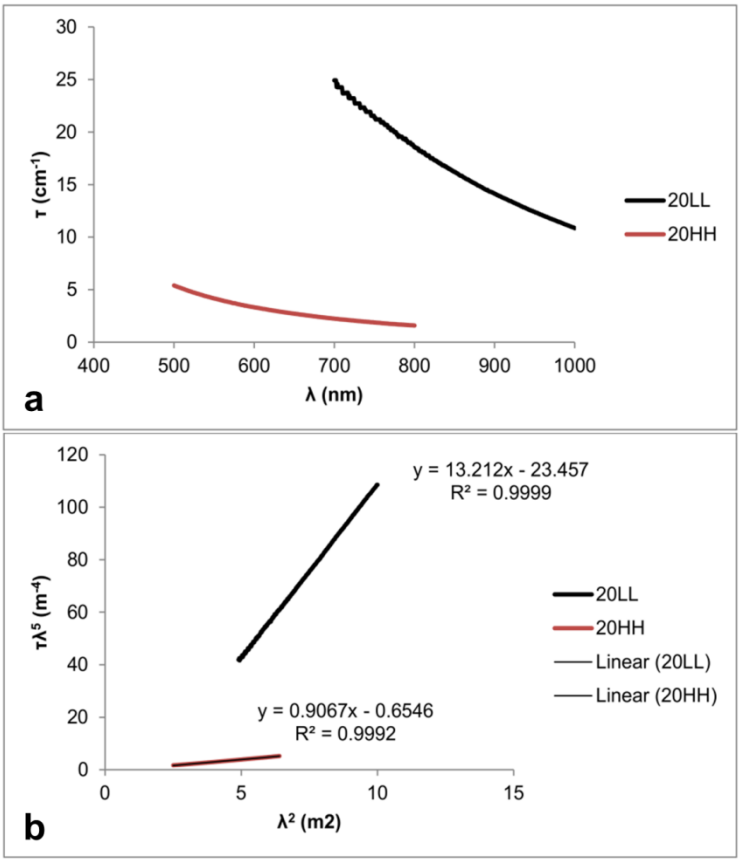

Fig. S1: (a) Data obtained from turbidity measurements for 20LL and 20HH compositions. Note the different spectral range used as a consequence of the high optical density of the 20LL hydrogel. (b)Turbidimetry analysis as explained earlier for the deduction of fiber structural parameters. Both samples show a linear response of $\tau\lambda^5$ *versus* λ^2.

B. Diffusivity of dextran molecules

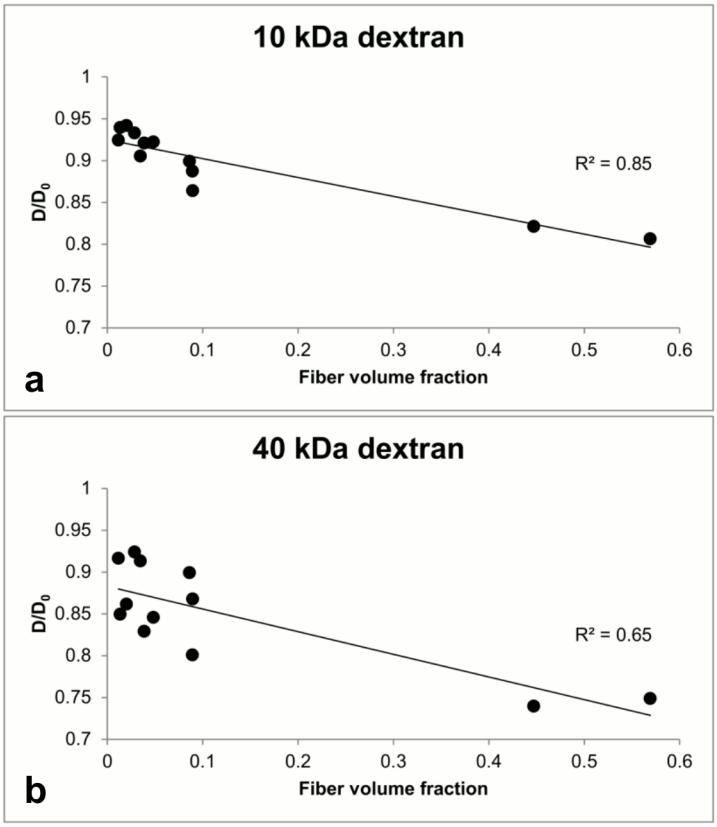

Fig. S2: Diffusivity of 10 (a) and 40 kDa dextran (b) with respect to the fiber volume fraction for all hydrogel compositions.

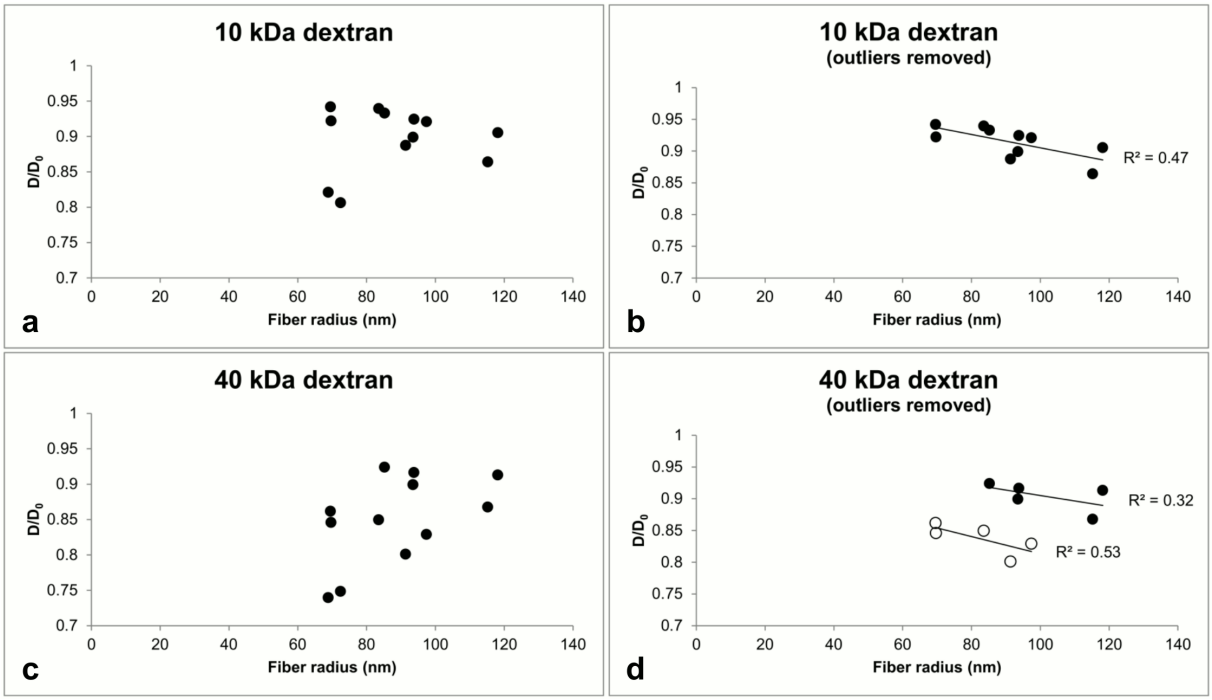

Fig. S3: Diffusivity of 10 (a and b) and 40 kDa dextran (c and d) with respect to the fiber radius for all hydrogel compositions (a and c) and all except the outliers 20LH and 20HH (b and d). Data in (d) are divided in a high-thrombin (empty circles) and a low thrombin concentration (solid circles).

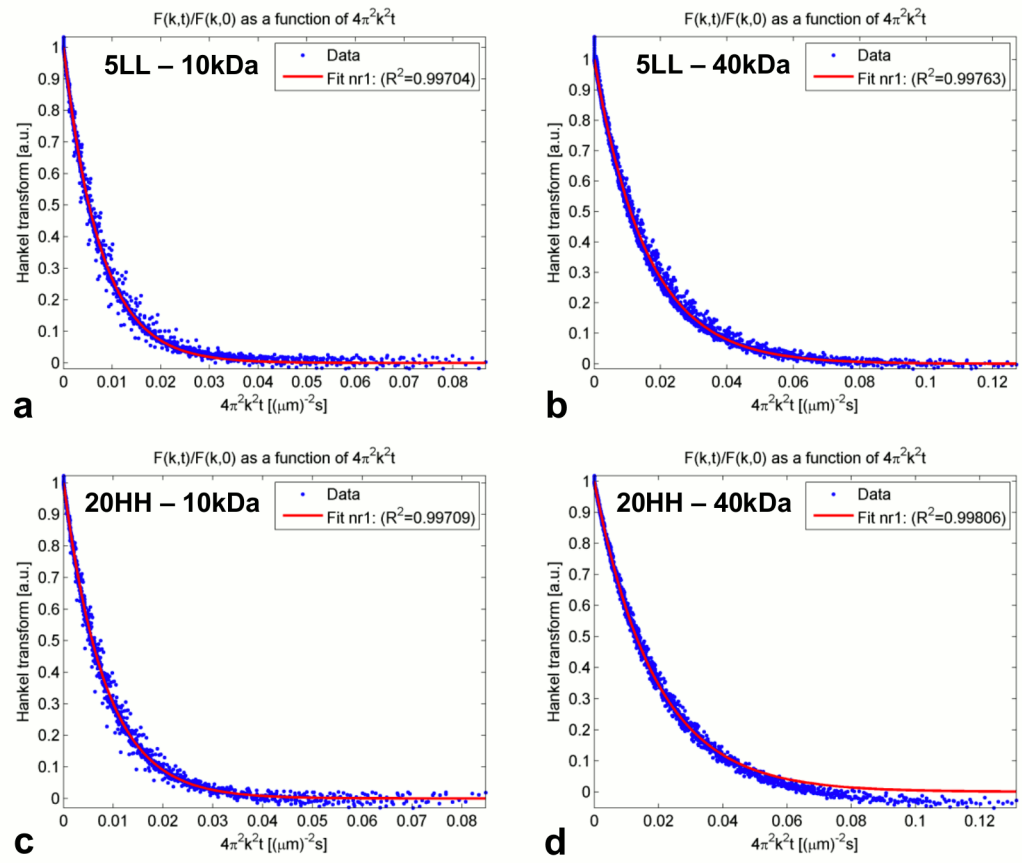

Fig. S4: Hankel transform and single exponential fit to the experimental data for the diffusion of 10 kDa (a and c) and 40 kDa dextran (b and d) in 5LL (a and b) and 20HH (c and d) hydrogels as obtained from the FRAP analysis program [51].

Estimation of the predicted relative diffusivities for impermeable fibers

Fibrin fibers exhibit intrafibrous porosity which is dependent on the polymerization conditions. For the purpose of assessing whether the Ogston model would be applicable for fibrin fibers which are hypothetically entirely impermeable, the following approximations were made. First, the internal fiber density was hypothesized to be equal to fibrinogen density (ρ_{fib} = 1395 mg/mL) for all compositions, and new values for the fiber volume fraction were calculated again using equation (5). Second, the network conformations were assumed to remain unchanged and new fiber radii were then approximated by the following relationship:

$$\rho_f V_f = \rho_{imp} V_{imp}$$

$$\rho_f \pi r_f^2 h = \rho_{imp} \pi r_{imp}^2 h$$

$$r_{imp} = \sqrt{\frac{\rho_f r_f^2}{1395}}$$

With ρ_{imp}, V_{imp} and r_{imp} the hypothetical fiber internal density, fiber volume and fiber radius of the impermeable fiber, respectively.

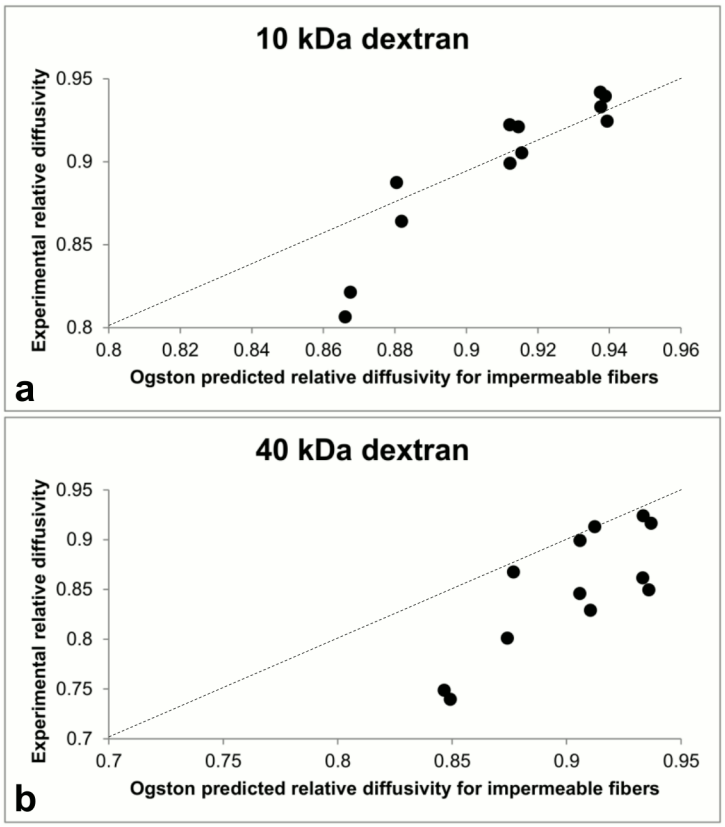

Fig. S5: Comparison of experimental relative diffusivity of dextran solutes in fibrin hydrogels with the predicted values from the Ogston model adapted for impermeable fibers. The dashed line has a slope equal to 1 (equal experimental and predicted values).

C. Shear rheology

The following calculations were performed using Matlab. Ġ was computed using a Savitzky–Golay filter (27-point window, cubic-spline approximation) on the raw G'-t curve and the maximum Ġ value was determined. The part of the Ġ curve lying to the right of the maximum was approximated by a two-term exponential decay function in order to determine t_s (Fig. S6). Due to the very small changes in obtained values over time this approximation was needed to find the actual time point with high precision.

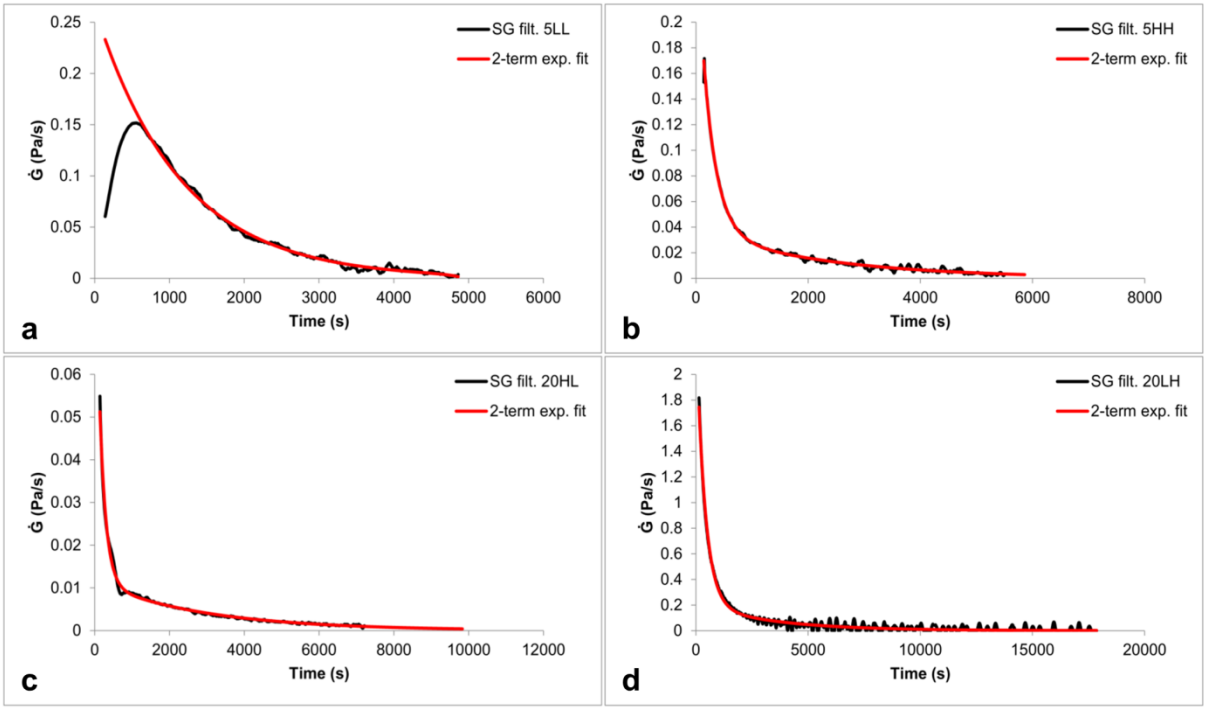

Fig. S6: Black lines indicate Ġ obtained by applying a Savitzky-Golay filter on averaged experimental G' results (data in Fig. 8a); red lines are a two-term exponential fit to the Ġ data.

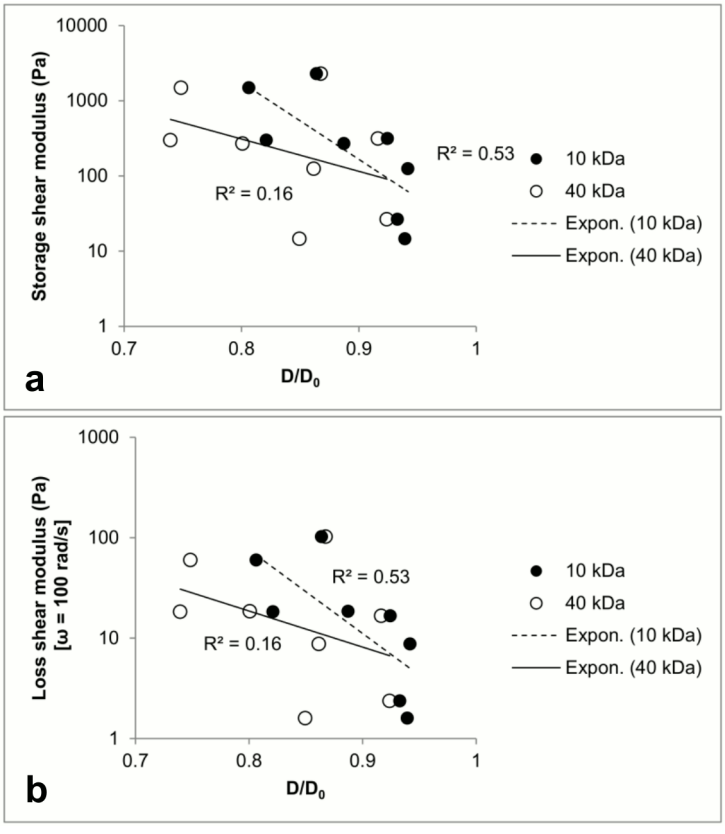

Fig. S7: (a) Storage shear modulus versus relative diffusivity and (b) loss modulus at high frequency (100 rad/s) versus diffusivity, for 10 kDa (solid circles) and 40 kDa (empty circles) dextran solutes.